



Soft Matter

Fabric-based jamming phase diagram for frictional granular materials

Journal:	<i>Soft Matter</i>
Manuscript ID	SM-ART-09-2023-001277.R2
Article Type:	Paper
Date Submitted by the Author:	n/a
Complete List of Authors:	Wen, Yuxuan; University of Colorado Boulder, Civil, Environmental and Architectural Engineering Zhang, Yida; University of Colorado Boulder, Civil, Environmental and Architectural Engineering

SCHOLARONE™
Manuscripts

Soft Matter

Guidelines for Referees

Thank you very much for agreeing to review this manuscript for [Soft Matter](#).



“An interdisciplinary journal focusing on innovative soft matter topics through original research and reviews”

Soft Matter has a global circulation and interdisciplinary audience with a particular focus on the interface between chemistry, physics, materials science, biology and chemical engineering. *Soft Matter* aims to publish significant advances reporting new soft matter materials or phenomena, encompass their design, synthesis, and use in new applications or provide fundamental insight and observations on their behaviour. Experimental, theoretical and computational soft matter approaches are encouraged.

The following manuscript has been submitted for consideration as a

FULL PAPER

The primary criterion for acceptance of a contribution for publication is that it must report significant advances and make a significant contribution to its field. *Soft Matter* is an **interdisciplinary** journal and suitable papers should cross disciplines or be highly significant within the field from which they originate.

When preparing your report, please:

- Focus on the **originality, importance, impact** and **reproducibility** of the science.
- Refer to the [journal scope and expectations](#).
- **State clearly** whether you think the article should be accepted or rejected and give detailed comments (with references) both to help the Editor to make a decision on the paper and the authors to improve it
- **Inform the Editor** if there is a conflict of interest, a significant part of the work you cannot review with confidence or if parts of the work have previously been published.
- **Provide your report rapidly** or inform the Editor if you are unable to do so.

Best regards,

Professor Alfred Crosby
Editor-in-Chief

Dr Maria Southall
Executive Editor

Contact us

Please visit our [reviewer hub](#) for further details of our processes, policies and reviewer responsibilities as well as guidance on how to review, or click the links below.



What to do
when you
review



Reviewer
responsibilities



Process &
policies

Response to the reviewers

The authors sincerely thank the reviewer #1 for carefully reexamine the revised manuscript. Hereafter, a point-by-point response is provided. The sections of the manuscript edited in accordance with the reviewers' comments are indicated with red fonts.

1. In line 30, "JPD" is not defined before this sentence.

Thanks for pointing it out. The JPD is now defined in line 30.

2. In line 173, Fig. 2(c) should be Fig. 2(b).

We thank the reviewer for catching this. It is now updated in line 173.

3. In line 203, $F_n^{viscous}$ and $F_t^{viscous}$ are not defined.

Thanks for reminding. $F_n^{viscous}$ and $F_t^{viscous}$ are now defined in the text line 195-197.

4. The authors added an explanation of the Cundall's numerical dumping. However, the description is too brief to understand it. Can the author explain the dumping by using equations?

Sure, the Cundall's damping equation is now introduced in Section 2.3, Eq. (4).

5. In the sentence containing Eq. (5), Ω is used as a scalar. However, I think $d\Omega$ means $\sin\theta d\theta d\phi$ in the spherical coordinates, and Ω is not a scalar.

Thanks for pointing it out. In original manuscript, we intend to show that the integration is conducted over the whole space in spherical coordinates (includes all polar angle and azimuth). We agree with the reviewer that $d\Omega = \sin\theta d\theta d\phi$, and the adoption of using Ω (and hence $d\Omega$) in Eq. (5) in the original manuscript is purely for simplicity purpose. Now we have updated the manuscript to use the polar angle and azimuth in equations. Please see Eqs. (6) and (7) in the revised manuscript.

6. In lines 342-347, the authors state that "the reliability of the obtained jamming threshold ϕ_F " is underscored based on the fitting of the data using Eq. (14) with $\phi_c = 0.5700$. But, I'm not sure

that this statement is correct because the fitting with different ϕ_c can be applied by choosing a_2 , b_2 , and $f_{nr, jam}$.

The ϕ_c is obtained using the fitting equation with the best-fit parameters that leads to the **highest** R-squared value. The parameters a_2 , b_2 and ϕ_c are all determined in this procedure and remain unchanged when the highest R-squared value is identified. Please see the paragraph after Eq. (15), the highest $R^2 = 0.9927$ is achieved with $a_2 = 0.3133$, $b_2 = 0.3215$ and $\phi_c = 0.5700$.

7. In line 460, something is grammatically wrong.

Thanks. It is corrected and updated, please see line 468-470.

8. In line 515, Fig. 10 should be Fig. 8.

Thank you. It has been updated, please see line 524.

9. In Fig. 3(b), the authors add the conceptual densest state line, but why does this line decrease monotonically with increasing p ? If there is any reason for this behavior, they need to mention it in the text.

In Fig. 3(b), p represents the mean stress inside the granular packing with the expression $p = \frac{1}{3} \sigma_{kk}$. The conceptual densest state line in the e - p plane shall decrease monotonically with the increasing p because of elastic deformation of the grains and contacts at higher stress levels (without considering grain breakage). We have updated the main text to mention this, please see the paragraph after Eq. (14).

Reference

- Chang, C. S., Deng, Y. & Yang, Z. (2017). Modeling of Minimum Void Ratio for Granular Soil with Effect of Particle Size Distribution. *Journal of Engineering Mechanics* **143**, No. 9, 04017060.
- Cubrinovski, M. & Ishihara, K. (2002). Maximum and minimum void ratio characteristics of sands. *soils and Foundations* **42**, No. 6, 65-78.
- Kanatani, K.-I. (1984). Distribution of directional data and fabric tensors. *International Journal of Engineering Science* **22**, No. 2, 149-164.
- Makse, H. A., Johnson, D. L. & Schwartz, L. M. (2000). Packing of Compressible Granular Materials. *Physical Review Letters* **84**, No. 18, 4160-4163.

- Maroof, M. A., Mahboubi, A., Vincens, E. & Noorzad, A. (2022). Effects of particle morphology on the minimum and maximum void ratios of granular materials. *Granular Matter* **24**, No. 1, 41.
- O'Hern, C. S., Silbert, L. E., Liu, A. J. & Nagel, S. R. (2003). Jamming at zero temperature and zero applied stress: The epitome of disorder. *Physical Review E* **68**, No. 1, 011306.
- Zhang, H. P. & Makse, H. A. (2005). Jamming transition in emulsions and granular materials. *Physical Review E* **72**, No. 1, 011301.

Fabric-based jamming phase diagram for frictional granular materials

Yuxuan Wen¹, Yida Zhang^{2*}

Abstract

Jamming phase diagram maps the phase states of granular materials to its intensive properties such as shear stress and density (or packing fraction). We investigate how different phases in jamming phase diagram of granular materials are related to its fabric structure via three-dimensional discrete element method simulations. Constant-volume quasi-static simple shear tests ensuring uniform shear strain field are conducted on bi-disperse spherical frictional particles. Specimens with different initial solid fractions are sheared until reaching steady state at a large shear strain (200%). The jamming threshold in terms of stress, non-rattler fraction, and coordination numbers (Z 's) of different contact networks are discussed. The evolution of fabric anisotropy (F) of each contact network during shearing is also examined. By plotting the fabric data in the F - Z space, a unique critical fabric surface (CFS) becomes apparent across all specimens, irrespective of their initial phase states. Through the correlation of this CFS with fabric signals corresponding to jamming transitions, we introduce a novel jamming phase diagram in the fabric F - Z space, offering a convenient approach to distinguish the various phases of granular materials solely through the direct observation of geometrical arrangements of particles. This jamming phase diagram underscores the importance of the microstructure underlying the conventional jamming phenomenon and introduces a novel standpoint for interpreting the phase transitions of granular materials that have been exposed to processes such as compaction, shearing, and other complex loading histories.

¹ Ph.D. Candidate, Dept. of Civil, Environ. and Architect. Eng., University of Colorado Boulder, Boulder, CO, USA.

² Assistant Professor, Dept. of Civil, Environ. and Architect. Eng., University of Colorado Boulder, Boulder, CO, USA.

* Corresponding author. Email: yida.zhang@colorado.edu

24 1 Introduction

25 Jamming is a phenomenon where amorphous disordered materials such as granular soils,
 26 colloidal suspensions, emulsions, and glasses transform from a fluid-like to a solid-like state
 27 and has been widely observed in nature and engineering practice. This abrupt transition is
 28 often described by a surface in the 3-dimensional (3D) space of temperature, load, and the
 29 inverse of density.¹ For granular materials which are athermal (i.e., the thermal fluctuation is
 30 insufficient to alter their packing configurations), the corresponding **jamming phase diagram**
 31 **(JPD)** becomes a 2-dimensional (2D) plane of shear stress τ vs. packing fraction ϕ .^{2,3} O'Hern
 32 and coworkers^{4,5} investigated the onset of jamming for frictionless granular packings by
 33 increasing density at zero shear stress and found that the jamming point J has a packing
 34 fraction ϕ almost identical to that of the random close packing, i.e., $\phi_J \approx \phi_{RCP} \approx 0.84$ in 2D,
 35 and $\phi_J \approx \phi_{RCP} \approx 0.64$ in 3D cases.

36 Frictional granular systems, however, could jam over a finite range of ϕ with ϕ_J being
 37 dependent on the sample preparation protocols and system parameters. For example, ϕ_J
 38 decreases when particle-particle friction coefficient μ increases or compression rate
 39 decreases.⁶⁻⁸ The random close packing ϕ_{RCP} is approximately the upper bound of ϕ_J for
 40 frictional granular systems.⁹ Song and coworkers¹⁰ analytically derived the minimum ϕ of 3D
 41 random loose packings $\phi_{RLP}^{\min} \approx 0.536$ and predicted it to be the theoretical lowest threshold of
 42 ϕ_J for isostatic jammed frictional granular materials if μ is infinitely large. This is supported
 43 by the observation that $\phi_{RLP}^{\min} \approx 0.536$ is close to the lowest stable ϕ ever reported for
 44 monodisperse spheres.¹¹ Therefore, a frictional granular packing with $\phi_{RLP}^{\min} < \phi < \phi_{RCP}$ can be
 45 either jammed or unjammed depending on its preparation protocol,¹² blurring the phase
 46 transition boundary depicted in classical JPDs.

47 Bi and coworkers⁹ conducted 2D pure shear tests on photoelastic disks isotropically
 48 compressed to initially unjammed states $\phi < \phi_J$. In their experiments, ϕ_J is closer to the upper

49 bound ϕ_{RCP} as their sample preparation involves gentle tapping which can break force chains,
50 release the friction buildups at contacts, and thus relax the system's stress to the lower values.
51 When shearing is followed, the specimen may stay unjammed, exhibit weak resistance to
52 shear, or develop strong shear stress depending on the initial ϕ . They have thus proposed two
53 more intermediate phases for frictional packings, namely the "fragile" and the "shear
54 jammed" phases, in addition to the unjammed and jammed phases depicted by the classical
55 JPD for frictionless systems. The fragile state is able to support loads only along the
56 compatible direction (i.e., the direction that strong force network percolates) without
57 undergoing plastic rearrangement.¹³ The shear jammed phase can resist perturbation in all
58 directions and thus is a truly jammed state induced by shear. Recently, Zhao and coworkers¹⁴
59 further enriched the generalized JPD⁹ by locating the boundaries between the unjammed, the
60 shear jammed, and the fragile states on the mean stress p vs. packing fraction ϕ plane via a
61 series of multiring Couette shear experiments on photoelastic disks.

62 While JPD offers a unifying framework to discuss the phase transition of granular
63 materials in terms of macroscopic variables (p , τ , ϕ), the underlying micro-mechanisms that
64 governs such transition can be only studied by tracking the microstructural evolution of the
65 granular assembly. Existing studies on JPD have extensively focused on the isotropic
66 measures of granular microstructure such as the coordination number Z ,^{5, 10} the non-rattler
67 fraction f_{nr} ,⁹ and the contact-force statistics.¹⁵⁻¹⁷ It has been found that frictional granular
68 materials will develop strong fabric anisotropy when subjected to shearing.¹⁸⁻²⁰ A series of
69 true triaxial Discrete Element Method (DEM) simulations shows that steady-state granular
70 flow is always anisotropic, the degree of which depends on the confining pressure and shear
71 mode.²¹ Recent DEM simulations investigating the flow-arrest transition^{22, 23} that is similar to
72 the shear-jamming have also revealed that fabric anisotropy is a crucial variable influencing
73 the transition between solid-like and fluid-like state. X-ray microtomography (X- μ CT)
74 observations of sheared sand specimens indicate that the macroscopic stress-strain behavior is
75 tightly related to the evolution of fabric anisotropy.^{24, 25} An important modification of the
76 classical critical state theory²⁶ is hence proposed to consider fabric anisotropy²⁷ for modeling

77 the quasi-static stress-strain response of granular soils.²⁸⁻³⁰ The characteristics of fabric
 78 anisotropy and its relationship with granular jamming have been explored in several previous
 79 studies.^{9, 14, 31} However, they fall short of considering fabric anisotropy as an essential
 80 variable in a JPD for distinguishing various phases including jammed, shear jammed, fragile,
 81 and others. This might be due to the intuition that a granular assembly develops trivial
 82 anisotropic microstructure at low mean stress levels, and a single scalar indicator such as Z
 83 would suffice for phase characterizations.

84 Our recent DEM experiments^{32, 33} have challenged this picture. Specifically, as shown in
 85 Fig. 1, we found unjammed (or “liquefied” in soil mechanics terminology) frictional granular
 86 specimens exhibits clear fabric anisotropy F with $p \approx 0$ maintained throughout under zero
 87 gravity condition. The F value of unjammed specimens is strongly correlated with the Z for
 88 the full range of $0 < Z < Z_{jam}$. This line smoothly joins the critical-state fabric data of jammed
 89 specimens ($Z > Z_{jam}$) and forms a unique *critical fabric surface* (CFS) in the F - Z plane (Fig.
 90 1a). Similar results have also been identified³⁴ where the pressure-controlled simulations lead
 91 to a CFS in the jammed region and a model is proposed for describing it. The CFS in Fig. 1a
 92 can also be visualized in the principal space of the fabric tensor (Fig. 1b) substantiated by
 93 data from true triaxial shear tests at different principal stress and strain ratios. Therefore, the
 94 CFS can be thought of as a universal attractor for all fabric states upon shearing, regardless of
 95 the shear mode and whether the sample is initially jammed or not. Moreover, on the fabric F -
 96 Z plane, one can reasonably distinguish the fabric paths and the portion of the CFS that
 97 belongs to samples that develop a finite shear stress at steady-state (jammed) and those do not
 98 (unjammed). This preliminary observation suggests that there may exist a one-to-one
 99 mapping between the conventional JPD in the τ - ϕ ^{5, 35-38} (or p - ϕ ^{9, 14}) plane and that in the
 100 fabric F - Z plane.

101 Motivated by the above, the objective of this paper is to: 1) systematically investigate the
 102 fabric characteristics of frictional granular materials near jamming transition; 2) develop a
 103 jamming phase diagram with fabric variables for the determination of phase state. Toward
 104 this goal, 3D DEM simulations of constant volume simple shear on bi-disperse frictional

105 spheres are conducted (Section 2). The stress-strain response and the jamming thresholds as
 106 well as the conventional JPD are discussed in Section 3. In Section 4, the fabric
 107 characteristics including Z and F for the non-rattler, total, and strong contact networks are
 108 explored and interpreted with reference to CFS, which leads to the development of a jamming
 109 phase diagram in F - Z space. Section 5 discuss the relationship between the fabric tensor and
 110 non-rattler fraction and Section 6 summarizes the main conclusions and discusses possible
 111 future extensions of this work.

112 **2 Methodology**

113 **2.1 Sample preparation**

114 The open-source DEM code YADE³⁹ is adopted to conduct constant volume simple shear
 115 numerical tests. In designing the simulation protocol, we have largely referred to the recent
 116 multiring Couette shear setup¹⁴ and formulated the following objectives: 1) be able to
 117 reproduce initially unjammed specimens with $\phi < \phi_J \approx \phi_{RCP}$; 2) preserve the uniform shear
 118 strain field across the specimen; 3) enforce the quasi-static condition; and 4) be able to shear
 119 to infinite shear strain. With these goals in mind, the details of the DEM simulation are
 120 reported below.

121 Each test consists of two stages namely sample preparation and simple shear. In the
 122 preparation stage, N spheres are generated sparsely without any contact enclosed in a
 123 rectangular prism with four periodic lateral boundaries and two rigid walls on the top and the
 124 bottom. To avoid crystallization,⁴⁰ binary mixture with particle diameter ratio $d_1 : d_2 = 1.4 : 1$
 125 and particle number ratio $N_1 : N_2 = 1 : 1$ is adopted.^{4, 8, 41} A compression procedure similar to
 126 Zhang and Maske⁷ is then applied, during which periodic boundaries and rigid walls moves
 127 inward with a constant rate (volumetric strain rate $\dot{\epsilon} = 0.05 \text{ s}^{-1}$) and stops when the specified
 128 ϕ is reached, followed by a relaxation step until p becomes stable (i.e., equilibrium). The total
 129 number of particles N is calculated such that the specimen reaches the specified ϕ with a
 130 dimension of $16d_1 \times 16d_1 \times 12d_1$ ^{37, 42} at the end of compression. Note that the spheres are set as

131 frictionless ($\mu = 0$) during the compression to mimic the tapping process adopted in the
 132 preparation of photoelastic specimens,^{9, 14} where friction buildups are effectively removed
 133 and the specimen is able to stay unjammed up to $\sim \phi_{RCP}$. Using this protocol, we have
 134 prepared a series of specimens with ϕ ranging from 0.45 to 0.64 at an increment of 0.01.
 135 After the specified ϕ is reached at the end of compression, μ is updated from 0 to 0.5, a
 136 typical value for frictional granular materials like sand.⁴³ This μ -adjusting technique is also
 137 commonly used in the granular mechanics community for obtaining specimens with different
 138 initial densities under the same confining pressure.⁴⁴⁻⁴⁶

139 2.2 Shearing algorithm

140 Before shearing, we agglomerated the particles located at the very bottom ($0 < z < 1.5d_1$)
 141 and top ($10.5d_1 < z < 12d_1$) of the specimen to form particle walls, as shown in Fig. 2(a).
 142 Shearing is performed through an athermal quasi-static (AQS) procedure^{47, 48}: first, a shear
 143 strain increment $\Delta\gamma$ is affinely imposed on each particle and the particle walls (Fig. 2(a)).
 144 This is followed by a relaxation stage where the system runs an additional N_t timesteps with
 145 shearing paused to allow dissipation of the kinetic energy (E_k) and return to equilibrium. The
 146 reason for adopting particle walls is to avoid slippage at the shear boundaries when the
 147 assembly is being relaxed. In addition, it reduces the overall complexity of contact type such
 148 that the contact within the whole granular system is consistent (i.e., particle-particle contact).
 149 It is important to distinguish our shear procedure from the conventional wall-driven
 150 mechanism, where shearing is induced solely by driving the walls, often resulting in non-
 151 uniform velocity field and strain localization in the specimen.⁴⁹⁻⁵¹

152 We have surveyed a range of N_t values and found that $N_t = 10$ can ensure the maximum
 153 E_k of the whole granular system in all simulations at the end of relaxation is sufficiently
 154 smaller than a kinetic energy threshold while offering a manageable simulation time to
 155 achieve $\gamma = 200\%$. This kinetic energy threshold is set to be $3 \times 10^{-4} m_1 g d_1$ where m_1 equals to
 156 the mass of a sphere with diameter d_1 and $g = 9.81 \text{m/s}^2$. The equivalent shear strain rate can
 157 be calculated by $\dot{\gamma} = \Delta\gamma / (N_t \Delta t)$ and is set to $0.5\% \text{ s}^{-1}$ (i.e., $\Delta\gamma = 0.05 \Delta t$ with Δt the value of a

158 single timestep) in all the simulations presented hereafter. Gravity is not activated in our
 159 simulation to maintain close analogy with the 2D multiring Couette experiments¹⁴ where all
 160 disks are placed horizontally.

161 The granular assembly sandwiched by the particle walls is the actual representative
 162 volume element (RVE) where the stress, strain, and fabric data are extracted. The effective
 163 height h of the sample is determined using the following procedure: the macroscopic shear
 164 stress can be calculated by summing all contact forces in the y direction on the top particle-
 165 wall divided by the cross-section area $\tau = \sum f_y / A$ where $A = 16d_1 \times 16d_1$. The average
 166 Cauchy stress can be also calculated according to the Love-Weber formula:⁵²

$$167 \quad \sigma_{ij} = \frac{1}{V} \sum_{c \in C} f_i^{(c)} l_j^{(c)} \quad (1)$$

168 where the sum is over all contacts C ; f the contact force; l the branch vector joining centers of
 169 the two particles at contact c ; V the volume of the specimen. For our simulations, the
 170 calculation of σ_{ij} in Eq. (1) should exclude the clumped particles in the C set and use the true
 171 specimen height h in calculating the specimen's volume $V = A \times h$. The applied τ is compared
 172 with the corresponding stress component σ_{zy} , and it is determined that $h = 9d_1 + 0.5d_2$ to have
 173 $\tau = \sigma_{zy}$ (Fig. 2(b)).

174 Note that Zhao and coworkers¹⁴ have reversed the shear direction after reaching the
 175 designated γ level to probe the stability of the developed force chain network, which was used
 176 to distinguish the fragile (F) and the shear jammed (SJ) states. Our study, however, is
 177 constrained by the available computational capability and the long simulation time of 3D
 178 assemblies. To avoid compromising the thoroughness of this simulation campaign (i.e.,
 179 reducing the total number of tests or shortening the maximum shear strain), we have opted to
 180 reserve the shear reversal tests for future studies, and focus the present analyses on the fabric
 181 signals of apparent jamming induced by monotonic shear without distinguishing the F and SJ
 182 states.

183 2.3 Contact model and parameters

184 The Hertz-Mindlin contact law⁵³ is adopted for our simulations. The normal force and
 185 tangential force with the consideration of Coulomb friction of a contact between particles 1
 186 and 2 are:

$$187 \quad F_n = \underbrace{\frac{4}{3} E_{eff} \sqrt{R_{eff}} \delta_n^2}_{F_n^{elastic}} + 2 \underbrace{\sqrt{\frac{5}{6}} \frac{\ln c_r}{\sqrt{\ln^2 c_r + \pi^2}} \sqrt{2m_{eff} E_{eff}} \sqrt{R_{eff}} \delta_n v_n}_{F_n^{viscous}} \quad (2)$$

$$188 \quad F_t = \min\left(\underbrace{8G_{eff} \sqrt{R_{eff}} \delta_t^2}_{F_t^{elastic}} + 2 \underbrace{\sqrt{\frac{5}{6}} \frac{\ln c_r}{\sqrt{\ln^2 c_r + \pi^2}} \sqrt{8m_{eff} G_{eff}} \sqrt{R_{eff}} \delta_t v_t}_{F_t^{viscous}}, \mu F_n\right) \quad (3)$$

189 where E is the Young's modulus; G is the shear modulus; R is the particle's radius; m is the
 190 particle's mass; c_r is the coefficient of restitution in the range of 0 to 1; μ is the Coulomb
 191 friction coefficient; δ_n , v_n and δ_t , v_t are the overlap distances and the relative velocities
 192 between the two contacting particles along the normal and tangential directions, respectively;

193 subscript '*eff*' represents effective variables, where $m_{eff} = \left(\frac{1}{m_1} + \frac{1}{m_2}\right)^{-1}$, $R_{eff} = \left(\frac{1}{R_1} + \frac{1}{R_2}\right)^{-1}$,

$$194 \quad G_{eff} = \left(\frac{2-\nu_1}{G_1} + \frac{2-\nu_2}{G_2}\right)^{-1} \quad \text{and} \quad E_{eff} = \left(\frac{1-\nu_1^2}{E_1} + \frac{1-\nu_2^2}{E_2}\right)^{-1} \quad \text{with } \nu \text{ being the Poisson's ratio;}$$

195 $F_n^{elastic}$ and $F_n^{viscous}$ represents the elastic and viscous term of the normal contact force
 196 respectively; $F_t^{elastic}$ and $F_t^{viscous}$ represents the elastic and viscous term of the tangential
 197 contact force respectively. The critical time step $\Delta t_{cr} = \min\left(R_i \sqrt{(\rho_g)_i / E_i}\right)$ is an important

198 factor that influences the simulation stability and speed, where subscript '*i*' represents the i^{th}
 199 particle³⁹. A safety factor 0.3 is further adopted such that $\Delta t = 0.3 \Delta t_{cr}$ to ensure the stability

200 of simulation. Table 1 lists the parameters used in the DEM simulations of this study. A
 201 relatively small value of E is adopted here to be able to use a relatively large time step.^{21, 54}

202 Our initial simulations have adopted the viscous term in this contact model. The
 203 computational time required to dissipate kinetic energy during the relaxation, however, was
 204 found to be excessively long. As a result, we adopted Cundall's numerical damping⁵⁵, shown
 205 in Eq. (4) and has already been implemented in YADE^{39, 56}, instead of the viscous damping

206 (i.e., setting $F_n^{viscous} = F_t^{viscous} = 0$) to accelerate the computation.

$$207 \quad \Delta \mathbf{F} = -\beta \operatorname{sign}(\mathbf{F} \cdot \mathbf{v}) \mathbf{F} \quad (4)$$

208 where \mathbf{F} = total force vector on a particle, \mathbf{v} = particle's velocity vector, β = Cundall's
 209 damping coefficient, $\Delta \mathbf{F}$ = damping force on a particle. The Cundall's numerical damping is
 210 implemented by introducing an additional force that is directly proportional to the total force
 211 exerted on a particle. This force aligns with the total force when the angle between the total
 212 force and the particle's velocity exceeds 90 degrees, and opposes the total force when the
 213 angle is smaller than 90 degrees.³⁹

214 **Table 1. Parameters in DEM simulations**

Parameters	Value
Grain density ρ_g	2650 kg/m ³
Particle diameter d_1	1.4 cm
Young's modulus E	200 MPa
Poisson's ratio ν	0.2
Friction coefficient μ	0.5
Cundall's damping β	0.2

215 2.4 Fabric tensor definition

216 The fabric structure of a granular packing can be quantified by the statistics of particle
 217 orientation,⁵⁷ void vector,⁵⁸ or contact normals.⁵⁹ For the spherical particles investigated in
 218 this study, we focus the fabric characterizations based on the contact network statistics.
 219 Consider the following directional distribution function of contact normals:⁵⁹

$$220 \quad \rho(\mathbf{n}) = \frac{2N_c}{N} \bar{\rho}(\mathbf{n}) \quad (5)$$

221 where \mathbf{n} is the unit contact normal vector; $\bar{\rho}(\mathbf{n})$ is the directional distribution density of
 222 contact normals; N and N_c are the total number of particles and contacts, respectively. The
 223 integration of $\rho(\mathbf{n})$ over all direction immediately gives the coordination number, Z :

$$224 \quad \int \rho(\mathbf{n}) d\Omega = \int \int \rho(\theta, \varphi) \sin \theta d\theta d\varphi = \frac{2N_c}{N} = Z \quad (6)$$

225 where Ω is the solid angle; θ is the polar angle; φ is the azimuth. The fabric tensor of the first

226 kind can be defined as:⁵⁹

$$227 \quad G_{ij} = \int \rho(\mathbf{n}) n_i n_j d\Omega = \int \int \rho(\theta, \varphi) n_i n_j \sin \theta d\theta d\varphi \quad (7)$$

228 where the trace of G_{ij} is exactly Z (i.e., $Z = G_{kk}$). In practice, G_{ij} can be calculated from the
229 discrete data of contact normals by:

$$230 \quad G_{ij} = \frac{2}{N} \sum_{k=1}^{N_c} n_i^{(k)} n_j^{(k)} \quad (8)$$

231 Alternatively, one can also approximate $\rho(\mathbf{n})$ by a second-order fabric tensor E_{ij} :⁵⁹

$$232 \quad \rho(\mathbf{n}) \approx \frac{1}{4\pi} E_{ij} n_i n_j \quad (9)$$

233 One can show that the mean spherical part of E_{ij} is Z (i.e., $Z = E_{kk} / 3$) by integrating Eq. (9)
234 over the whole spherical surface (i.e., $\theta \in [0, \pi]$ and $\varphi \in [0, 2\pi]$). It is also possible to express E_{ij}
235 in terms of G_{ij} by multiplying Eq. (9) with $n_k n_l$ and integrating over the whole spherical
236 surface,

$$237 \quad E_{ij} = \frac{15}{2} \left(G_{ij} - \frac{1}{5} G_{kk} \delta_{ij} \right) \quad (10)$$

238 The deviatoric part of E_{ij} follows:

$$239 \quad F_{ij} = E_{ij} - \frac{1}{3} E_{kk} \delta_{ij} \quad (11)$$

240 Substituting Eq. (11) into Eq. (9) gives:

$$241 \quad \rho(\mathbf{n}) \approx \frac{1}{4\pi} \left(Z + F_{ij} n_i n_j \right) \quad (12)$$

242 which can be viewed as the spherical harmonic expansion of $\rho(\mathbf{n})$ truncated to the second
243 order⁵⁹. In all of our simulations, the mean fabric will be monitored by tracking the
244 coordination number ($Z = E_{kk} / 3$) and the fabric anisotropy will be characterized by the
245 second invariant of F_{ij} , i.e., $F = \sqrt{(3/2) F_{ij} F_{ij}}$. The normalized fabric anisotropy is defined as
246 the ratio between fabric anisotropy and the coordination number: $\bar{F} = F / Z$.

247 Note that the contact-based fabric measures strongly depend on how one defines the
248 contact network. Past studies on granular jamming usually exclude “rattlers” which are
249 particles that do not participate in the load-bearing network and only inspect the contact

250 statistics of non-rattler particles. While the physical definition of rattler is unique (i.e., relying
 251 on constraint counting or inspecting if the central particle can move freely with neighboring
 252 particles fixed), the practical implementations for identifying rattlers vary across different
 253 studies. This variation includes considering particles with contact numbers less than one,^{41, 60,}
 254 ⁶¹ two,^{9, 14, 62, 63} three,⁶⁴ and four,⁶⁵ reflecting different criteria adopted for the purpose of
 255 simplicity. Here we adopt the implementation with the contact number less than 2 to be
 256 consistent with that in simple/pure shear tests of photoelastic disks,^{9, 14} in calculating the
 257 fabrics of the non-rattler contact network. An iterative method that was recently developed⁶⁶
 258 and closely aligned with the method originally proposed for jamming in hard sphere
 259 packings⁶⁷, offers a notably more rigorous approach to identifying rattler and may be adopted
 260 in future studies. Alternatively, fabric tensor defined based on the total contact network can
 261 be useful for granular system at very loose packings near the granular gas state. In such
 262 condition, most particles become rattler, and Eq. (5) becomes ill-defined for the non-rattler
 263 contact network but is still valid for the total contact network. Finally, the total contact
 264 network can be decomposed into two subnetworks of strong contacts and weak contacts.¹⁹
 265 The strong contacts carry a net force f larger than the average contact force of the whole
 266 network $\langle f \rangle$ while $f < \langle f \rangle$ for weak contact network. In this study, fabric tensors of the
 267 non-rattler, the total, and the strong contact networks are all investigated, and they are
 268 marked with subscripts “ nr ”, “ t ”, and “ s ”, respectively. Note that the value of N is set as the
 269 number of non-rattler particles (N_{nr}) in calculating the non-rattler fabric tensor in Eq. (5),^{9, 14}
 270 while N is the number of all particles for calculating the total- and the strong- contact fabric
 271 tensors.^{32, 33}

272 **3 Jamming thresholds**

273 **3.1 Stress space**

274 When investigating the jamming phenomena, a crucial step is to ascertain the jamming
 275 thresholds, which can be defined in relation to ϕ , p , and f_{nr} , etc. Fig. 3(a) presents the mean
 276 stress $p = \sigma_{kk}/3$ of all specimens during steady state (also known as the “critical state”)

277 shearing. Notably, the relationship between critical state mean stress (p_c) and ϕ exhibits an
 278 opposite trend clearly distinguished at $\phi = 0.57$, and the error bar in $\phi < 0.57$ is higher than
 279 that in $\phi > 0.57$. When $\phi \geq 0.57$, p_c diminishes with ϕ in a power-law relationship as ϕ
 280 decreases, which can be described as:⁷

$$281 \quad \frac{p_c}{p_a} = a_1 (\phi - \phi_c)^{b_1} \quad (13)$$

282 where p_a is the atmosphere pressure (101.3kPa), a_1 , b_1 and ϕ_c are the fitting parameters. The
 283 best-fit results, yielding the highest R^2 value of 0.9943, indicate $a_1 = 154.6031$, $b_1 = 1.1770$,
 284 and $\phi_c = 0.5700$, are shown in the subplot of Fig. 3(a). Note that these parameters are system
 285 and protocol dependent.¹² The calibrated ϕ_c serves as the threshold to distinguish between
 286 shear jammed (including fragile) and unjammed specimens within our system. For
 287 consistency with the Couette shear experiment we are simulating,¹⁴ this threshold will be
 288 denoted as ϕ_F . At $\phi_F = 0.57$, $p_c = 3$ kPa, hence, a noise threshold $p_{noise} = 3$ kPa is identified and
 289 adopted as a criterion to determine whether a packing is shear jammed (including fragile)
 290 during monotonic shearing.¹⁴ The implementation of p_{noise} represents a simplified approach to
 291 determine jamming. It is important to note that the transition between jamming and
 292 unjamming is notably intermittent and stochastic, characterized by pronounced finite size
 293 effect.^{22, 68} The shear strain needed for p to reach p_{noise} (jamming) exhibits increasing
 294 divergence as ϕ decreases and deviates from ϕ_J . When subjected to a larger shear strain, p
 295 may attain the specified p_{noise} for specimen with a smaller ϕ , indicating a shift in the onset of
 296 shear jamming. This implies the assigned value of p_{noise} might vary with changes in system
 297 size. Understanding these statistical uncertainties is pivotal for precisely defining the
 298 boundary between jammed and unjammed states, and these aspects need to be thoroughly
 299 investigated in future studies.

300 Fig. 3(b) displays the so-called ‘‘critical state line’’ (CSL) on e - p plane, where e is the void
 301 ratio defined as the void volume over the solid volume and is related to ϕ by $e = (1-\phi)/\phi$. In
 302 critical state soil mechanics,⁶⁹ only the data in the jammed region is considered, and the
 303 expression of CSL is:

$$e_c = e_r - \lambda \left(\frac{p}{p_a} \right)^\xi \quad (14)$$

305 where e_r , λ and ξ are the fitting parameters. Their values are 0.7597, 0.0540 and 0.6644
 306 respectively for the current system. Following the compression protocol in Section 2, the
 307 isotropic jamming point is detected at $\phi_J = 0.638 \approx \phi_{RCP}$ with an initial p slightly exceeds
 308 p_{noise} . We noted that it is impossible to generate an isotropic specimen passing this point ($\phi >$
 309 ϕ_J or $e < e_J$) without maintaining a finite pressure ($> p_{noise}$) on the boundary. Thus, on the
 310 same e - p plane, there should be a densest state line (DSL) that no specimen's (e , p) data can
 311 exist below it. This conceptual line is sketched in Fig. 3(b). **The DSL should be**
 312 **monotonically decreasing, as the achievable densest state should have smaller void ratio e at**
 313 **higher mean stress levels p due to elastic deformation of the grains and contacts.** The (e , p)
 314 state of the packing should always evolve above this DSL, influenced by particle attributes
 315 such as stiffness and morphology (including shape and grain size distribution). A state falling
 316 below the existing DSL should require changes in the geometrical characteristics of the
 317 particles through processes like grain crushing and asperity breakage, etc. The concept of
 318 DSL aligns closely with the notion of minimum void ratio e_{min} which is an impact index for
 319 defining granular soils' relative density and compactness in geotechnical engineering.⁷⁰⁻⁷²
 320 The precise determination of DSL and its correlation with particle stiffness and morphology
 321 exceeds the scope of this paper.

322 Fig. 3(c) and (d) presents stress-strain evolution and stress paths in τ - ϕ and q - p plane of
 323 shear jammed specimens with $\phi \geq \phi_F$. It shows that stress becomes stable around $\gamma = 1.6 \sim 2.0$.
 324 Consequently, the properties of the specimens at the steady/critical state are determined by
 325 averaging their values within this γ range, thereby mitigating the influence of data oscillation
 326 in DEM simulations. Fig. 3(d) demonstrates that all shear jammed specimens converge to the
 327 same critical state stress ratio $\eta_c = 0.61$.

328 **3.2 Non-rattler fraction**

329 Non-rattler fraction f_{nr} is defined as the ratio between the number of non-rattler particles
 330 (N_{nr}) and the number of total particles (N). Fig. 4(a) presents the evolution of f_{nr} during

331 shearing. It is observed that: 1) the specimen with $\phi = 0.64$ is initially jammed and has a f_{nr}
 332 larger than a reference value 0.855 prior to shearing; 2) For initially unjammed specimens
 333 with $\phi = 0.45\sim 0.63$, f_{nr} increases as the shear strain accumulates, and only those shear
 334 jammed (including fragile) with $\phi \geq \phi_F = 0.57$ has f_{nr} reach or exceeds 0.855 at steady state (γ
 335 = 1.6 ~ 2.0). These findings suggest that the special value of $f_{nr, jam} = 0.855$ can serve as a
 336 criterion to separate unjammed and (shear) jammed states, regardless of the initial phase of
 337 the specimen. A similar threshold $f_{nr, jam} \approx 0.83$ is reported for 2D granular disk assemblies in
 338 pure shear experiments.¹⁴ However, this does not imply that $f_{nr, jam}$ is a universal value across
 339 various system configurations. Instead, it is contingent on system parameters such as grain
 340 size distribution, contact model, interparticle friction coefficients, preparation protocols,
 341 system sizes, etc.

342 The steady-state values of non-rattler fraction $f_{nr, st}$ are plotted in Fig. 4(b) with the error
 343 bar indicating the fluctuation of f_{nr} in the range of $\gamma = 1.6 \sim 2.0$. It is observed that f_{nr}
 344 fluctuates significantly for very loose specimens with $\phi = 0.45 \sim 0.50$, a sign of highly
 345 unstable fabric structure despite the specimen has undergone a long time of shearing. In
 346 contrast, the error bar of $f_{nr, st}$ reduces considerably for medium loose specimens with $\phi = 0.51$
 347 ~ 0.56 < ϕ_F , meaning that a relatively stable fabric structure is developed at steady state for
 348 unjammed medium loose specimens. Specimens with $\phi \geq \phi_F = 0.57$ are all jammed during
 349 shear and have negligible error bar associated with their $f_{nr, st}$ data. Similar to Fig. 3(a), the
 350 evolution trend diverges at ϕ_F , and $f_{nr, st}$ vanishes as ϕ decreases following a power law pattern
 351 when $\phi \geq \phi_F = 0.57$. An equation similar to Eq. (13) with $f_{nr, jam} = 0.855$ is proposed:

$$352 \quad f_{nr, st} - f_{nr, jam} = a_2 (\phi - \phi_c)^{b_2} \quad (15)$$

353 and the best-fit parameters yielding $R^2 = 0.9927$ are $a_2 = 0.3133$ and $b_2 = 0.3215$ and $\phi_c =$
 354 0.5700, as shown in the subplot in Fig. 4(b). The minimal disparity observed in the calibrated
 355 jamming- ϕ values between Fig. 3(a) and Fig. 4(b) underscores the consistency and robustness
 356 of the results, as well as the reliability of the obtained jamming threshold ϕ_F .

357 **3.3 Classical jamming phase diagram**

358 The JPD in the τ - ϕ plane is presented in Fig. 5(a) by taking the steady state shear stress τ as

359 the yield stress for each ϕ . The value of τ at jamming-unjamming transition gradually
 360 increases with ϕ as expected. The two previously identified special values for ϕ are marked,
 361 namely $\phi_F = 0.57$ where shear jamming occurs and $\phi_J = 0.638$ where isotropic jamming
 362 occurs.

363 It is worth noting that the original definition of fragile¹³ – “The inability to elastically
 364 support some infinitesimal loads along the incompatible directions” – is a highly conceptual
 365 one. Quantitative measures must be adopted to practically observe fragility and distinguish it
 366 from shear jamming in experiments. In some studies⁹, a granular packing is defined as fragile
 367 or shear jammed when the strong contact network percolates in only one direction or in all
 368 directions, respectively. This visual-based criterion can be ambiguous depending on how one
 369 perceives percolation. In other studies¹⁴, the fragile and shear jammed states are defined by
 370 whether p falls below or above p_{noise} , respectively, during the first loading reversal. This can
 371 introduce arbitrariness as well, as medium-loose granular packings may still resist shear
 372 during the first few cycles of stress reversal but have p drops to 0 in the subsequent cycles
 373 under undrained (i.e., constant ϕ) condition. This is a well-studied phenomenon called “cyclic
 374 liquefaction” in the soil mechanics literatures.^{32, 33, 73, 74} Therefore, the concept of fragile and
 375 its boundary with respect to the shear jammed state in JPD remains somewhat ambiguous and
 376 worth further investigation.

377 On the other hand, several studies^{9, 14, 75} suggested that there is a curved boundary
 378 between the jammed and shear jammed phases in τ - ϕ plane at $\phi > \phi_J$ regime. This may be
 379 inherited from the unjammed-jammed boundary in the original JPD for frictionless particles,^{1,}
 380³⁵ and implies that an initially jammed specimen can transit to shear jammed state when
 381 sheared under constant ϕ . It is however not at all clear what macroscopic signals correspond
 382 to this transition. To avoid ambiguity, a straight vertical line at ϕ_J is regarded as the
 383 boundary between the jammed and the shear jammed phases in Fig. 5, since specimens with
 384 $\phi_F \leq \phi < \phi_J$ in our simulation are initially unjammed but can be jammed under the
 385 introduction of shear stress, and the packing with $\phi \geq \phi_J$ is isotropically jammed before
 386 shearing. To summarize, in τ - ϕ plane (Fig. 5(a)), we define: (1) specimens falling within the

387 range of $\phi_F \leq \phi < \phi_J$ and $\tau < \tau_{yield}$ as belonging to the fragile or shear jammed state (F/SJ); (2)
 388 region of $\phi \geq \phi_J$ and $\tau < \tau_{yield}$ as jammed (J); (3) the rest as unjammed (UJ).

389 The JPD in the p - ϕ plane is presented in Fig. 5(b). It exhibits a similar boundary between
 390 the UJ and the F/SJ phases as the one identified in ref. 14. Here we have further enriched the
 391 diagram by considering the $\phi > \phi_J$ regime and adding the conceptual DSL discussed in Fig.
 392 3(b) after axes transformation. The region beyond DSL cannot be accessed unless processes
 393 such as particle breakage starting to alter the grain size distribution and the grain morphology
 394 of the specimen.⁷⁶⁻⁷⁸ Comparing Fig. 3(b) with Fig. 5(b), it is instructive to see that the well-
 395 established CSL in soil mechanics literature is essentially the same as UJ to F/SJ phase
 396 boundary in JPD. This equivalence permits the cross comparison between existing studies in
 397 both communities, which may inspire new directions of granular mechanics/physics research.
 398 In what follows, we inspect the fabric states of all tested specimens in an attempt to identify
 399 the microstructural patterns that control the phase transition of granular materials.

400 **4 Jamming phase diagram in fabric space**

401 **4.1 Fabric evolution**

402 The non-rattler, total-, and strong- contact coordination numbers (i.e., Z_{nr} , Z_t and Z_s) and
 403 fabric anisotropies (i.e., F_{nr} , F_t and F_s) in the simulations are presented in Fig. 6. The left
 404 figures show the evolution of Z 's with respect to γ . It is observed that the Z 's of specimens
 405 with $\phi = 0.45 \sim 0.63$ (initially unjammed) gradually increase to steady state, while the Z 's of
 406 initially jammed sample ($\phi = 0.64$) evolve to a steady state lower than the initial value. Just as
 407 in the preceding section where we established the jamming threshold as $p_{noise} = 3$ kPa and f_{nr}
 408 = 0.855, we now adopt the steady state Z value of specimens with $\phi = 0.57$ as the jamming
 409 threshold (Z_{jam}) to distinguish between unjammed and jammed states.

410 The right figures show the evolution of F 's with respect to γ . Since the specimens are
 411 initially isotropic, all F 's start at zero. The F_{nr} exhibits significant oscillations for unjammed
 412 specimens during initial shearing, which is expected as only a few contacts present at that
 413 stage and most particles are rattlers. The F_{nr} eventually stabilizes and reaches a steady state,

414 with value being lower for denser specimens. The steady-state F_t decreases slightly with ϕ
 415 when specimen is jammed ($\phi \geq \phi_F$) and increases moderately with ϕ when specimen is
 416 unjammed ($\phi < \phi_F$), while the steady-state F_s is always higher for larger ϕ specimens,
 417 consistent with our previous findings.^{32, 33} Note that the specimens of $\phi < 0.57$ have never
 418 been jammed at any stage of shearing but still has finite F_{nr} and F_t . This reveals an important
 419 but often neglected property of frictional granular materials: even loose quasi-static granular
 420 flow exhibiting $p \approx 0$ can develop distinct fabric anisotropy amid the dynamic creation and
 421 destruction of contact network after sufficient shearing. The fabric structure of unjammed
 422 granular systems has only gained some attention recently. In soil mechanics research, non-
 423 trivial fabric anisotropy in liquefied ($p \approx 0$) granular soils during continuous shearing has
 424 been recently observed.^{32, 33, 79} Studies on concentrated granular suspensions have also
 425 reported the development of anisotropic microstructure when shear is applied.⁸⁰ Augmented
 426 by our present observation that all specimens (UJ, F/SJ, and J) demonstrate finite F_{nr} and F_t
 427 after undergoing adequate shearing, it is justifiable to conclude that a steady-state granular
 428 flow consistently maintains microstructural anisotropy. This point will be further elaborated
 429 in the next section.

430 **4.2 Fabric path and critical fabric surface**

431 Fig. 7 presents the evolution path of fabric data throughout shearing ($\gamma = 0.0 \sim 2.0$) in the
 432 left plots and the steady-state fabric data (after the sample reaching steady-state shearing, $\gamma =$
 433 $1.6 \sim 2.0$) in the right plots on the F - Z plane. It is observed from Figs. 7(a)(c)(e) that the
 434 fabric paths of initially unjammed specimens ($\phi < 0.63$) always start at their minimum values
 435 (2 for Z_{nr} , 0 for Z_t and Z_s and F_t and F_s). The initial F_{nr} is quite scattered since the specimens
 436 near the extreme of $f_{nr} \rightarrow 0$ do not have a stable non-rattler contact network yet, and the
 437 occasional percolation of force chains along certain direction is registered as high initial F_{nr}
 438 values. Shearing drives their fabric paths towards higher Z value and eventually ceases
 439 evolving around the steady state (Z_{st} , F_{st}) identified in Figs. 6. For the initially jammed
 440 specimen ($\phi = 0.64$), its fabric paths start at a large coordination number ($Z_{nr} = 6.79 > Z_{nr, jam}$,
 441 $Z_t = 6.72 > Z_{t, jam}$, $Z_s = 2.78 > Z_{s, jam}$) with negligible anisotropy due to the initial isotropic

442 compression. During the course of shear, the values of its F 's ascend to their peak and
 443 subsequently drops to reach the CFS defined later, a trend concurrent with the reduction
 444 followed by an increase in the values of Z .

445 Figs. 7(b)(d)(f) presents only the steady-state fabric data ($\gamma = 1.6 \sim 2.0$). All three types of
 446 fabric measures clearly exhibit a steady-state fabric envelope on the F - Z plane. They are
 447 referred to as the Critical Fabric Surface (CFS) hereafter to be consistent with Fig. 1 and our
 448 previous works.^{30, 32, 33} Different types of equations are tried to capture the steady state fabric
 449 data. The power-law function (Eq. (16)) and the Gurnary function⁸¹ (Eq. (17)) are adopted to
 450 best fit the CFS of the non-rattler, total-, and strong- contact fabrics respectively for their
 451 simplicity as well as the relatively high R^2 values achieved.

$$452 \quad f(x) = a_3 x^{b_3} \quad (16)$$

$$453 \quad f(x) = x / (c_1 + c_2 \sqrt{x} + c_3 x) \quad (17)$$

454 The parameters for the best-fit CFS expressions are $a_3 = 12.18$ and $b_3 = -0.8557$ for non-
 455 rattler CFS with $R^2 = 0.9765$; $c_1 = 0.7674$, $c_2 = -0.8659$ and $c_3 = 0.584$ for total contact CFS
 456 with $R^2 = 0.9755$; $a_3 = 1.845$ and $b_3 = 0.6976$ for strong contact CFS with $R^2 = 0.9960$.

457 Fig. 7(d) indicates that the steady-state fabric anisotropy of total contact network $F_{t, st}$
 458 diminishes as Z_t approach to zero. It is therefore conceivable that in extremely loose packings
 459 (e.g., granular gas), particles will barely touch each other throughout quasi-static shearing,
 460 and the contact based CFS will no longer be descriptive of the material's fabric. To
 461 investigate this, an additional set of tests are conducted on extremely loose samples ($\phi < 0.45$)
 462 and observed that the fabric information was no longer reflected in CFS when $\phi = 0.40$. For
 463 the non-rattler CFS in Fig. 7(b), the data of $\phi = 0.40$ is highly scattered with $F_{nr, st}$ is in the
 464 range of $4 \sim 12$ and $Z_{nr, st}$ lies near the minimum value 2. In this case, only a few local non-
 465 rattler fabric clusters exist, and the calculated fabric tensor will be no longer representative
 466 for the whole packing. For the total- and the strong- contact CFS in Figs. 9(d) and (f), the
 467 data of $\phi = 0.40$ locates around the origin, meaning the fabric structure is hardly detectable
 468 even if external energy is continuously supplied by shearing. **From this purely geometrical**

469 standpoint, a ϕ_G that exists in the range of $0.40 \leq \phi < 0.45$ may be defined to separate the
 470 granular gas (G) and the granular liquid (UJ) regimes, in analogues to $\phi_F = 0.57$ and $\phi_J =$
 471 0.638 that respectively distinguishes the UJ to F/SJ and F/SJ to J transitions in the JPD in Fig.
 472 5. Our earlier speculation in Section 4.1 can now be put in stricter terms: steady-state
 473 granular flow with $\phi > \phi_G$ is always microstructurally anisotropic with non-zero Z 's,
 474 regardless of whether it is initially jammed or unjammed.

475 It is worth noting that the present DEM simulations are drastically different from authors'
 476 previous studies^{32, 33} in terms of the shear mode (simple shear vs. triaxial shear), contact
 477 model (Hertz-Mindlin vs. linear), grain size distribution (bi-disperse vs. polydisperse), and
 478 the control mechanism (athermal quasi-static shear vs. boundary-only control), yet the shapes
 479 of the obtained CFS's are surprisingly similar. Indeed, the total- and strong- contact CFS in
 480 Figs. 7(d)(f) and previous works^{32, 33} are all satisfactorily described by Eqs. (16) and (17)
 481 with slightly different parameters, respectively. Therefore, the unifying power of CFS lies in
 482 that it describes the steady-state fabric of all specimens regardless of their phase states, and is
 483 also robust and insensitive to the shear mode. Different portions of CFS host the steady-state
 484 fabric data of samples with different packing fractions denoted by different colors in Figs.
 485 7(b)(d)(f). This hints that there exists a direct relation between the UJ – F/SJ phase boundary
 486 on the JPD and the CFS in the F - Z plane, and possibly a one-to-one mapping between
 487 different phases and the regions surrounding CFS. We shall explore this in the next section.

488 4.3 Jamming phase diagram in fabric space

489 By inspecting the fabric paths in Fig. 7, we map the granular phases defined in Fig. 5 to
 490 the fabric F - Z plane for the non-rattler and the total contact networks in Fig. 8. The strong-
 491 contact plot is omitted since its shape is qualitatively similar to that of the total-contact plot.
 492 It features the following regions:

- 493 (1) The entire CFS and its immediate vicinity forms a narrow band collecting the steady-state
 494 fabric data, thus it is denoted as the “Flow steady” region.
- 495 (2) Samples with Z smaller than Z_{jam} and F above CFS are macroscopically identified as
 496 unjammed (i.e., $p \approx 0$). Their microstructures are still evolving with respect to γ (see Figs.

497 6(b) and (d), $\gamma = 0\sim 0.8$) and have not arrived at the CFS yet. Correspondingly, this region
 498 is denoted as “Flow transient” marked by the light gray color in Fig. 8. In this stage, the
 499 initial fabric induced by the preparation protocol is still being “remembered” by the
 500 specimen, and the term “transient” here refers to the microstructure being in transition to
 501 a new steady-state configuration driven by quasi-static shear γ . This term therefore should
 502 not be confused with the transient processes discussed in dynamic settings where time is
 503 the driving variable. The fabric paths of all UJ specimens ($\phi < \phi_F$) evolves within the
 504 Flow transient region and end at the Flow steady portion left to the Z_{jam} line.

505 **(3)** For F/SJ specimens ($\phi_F \leq \phi < \phi_J$), their fabric path will travel through the “flow transient”
 506 region, pass the Z_{jam} line, enter the “F/SJ” region marked by the red and green color, and
 507 finally reach the joint area of the “Flow steady” and the “F/SJ” regions. Although the
 508 fragile and shear jammed states are not distinguished in the present study, we hypothesize
 509 that specimens jammed at low Z values are more likely to be fragile and those reach
 510 relatively high Z are shear jammed. This is supported by the original definition of
 511 fragile¹³ that force chain inside the granular packing is percolated along one direction but
 512 is disconnected along the other direction, which corresponds to high F but low Z values.
 513 The exact boundary between the F and the SJ phases still needs to be systematically
 514 investigated in the future.

515 **(4)** The possible fabric states of jammed specimens ($\phi \geq \phi_J$) are marked by the dark gray zone
 516 based on the data in Fig. 7 and complemented by Fig. 1(a). The fabric states of jammed
 517 specimens eventually reach the “Flow steady” region at very high Z values as γ
 518 accumulates. Some overlap between the jammed and the SJ phases appear. This suggests
 519 that the same fabric state (Z, F) can be reached by specimens with different ϕ and phase
 520 states. Such overlapping could be attributed to the inability of the second-order fabric
 521 tensor E_{ij} in representing the full fabric information of a granular specimen. Comparing
 522 the higher-order fabric components or directly the $\rho(\mathbf{n})$ in the joint SJ-J regions may
 523 reveal the differences between the fabric structures of the two specimens.³³

524 There are also some blank zones in Fig. 8 where no fabric data from the present

525 simulation campaign are found. These zones are labeled as ‘A’, ‘B’ and ‘C’. Our previous
 526 study^{32, 33} and new simulations not reported here suggest that fabric states can indeed exist in
 527 region ‘B’ by stress reversals. For example, by performing unloading on a specimen in the
 528 ‘F/SJ’ or ‘Flow steady’ regions, the coordination number remains similar, but fabric
 529 anisotropy drops, and the fabric path moves downward to ‘B’. When cyclic stress reversal is
 530 applied on initially jammed specimens, Z will gradually decrease and the phase state moves
 531 leftward to region B.³³ We also found that preparing specimens at $\mu > 0$ permits an initially
 532 jammed state at a relatively loose packing $\phi_J < \phi_{RCP}$.³² This puts the specimen’s initial fabric
 533 state in region B directly, and shear drives the fabric path across region B and reaches CFS
 534 (Fig. 1(a)).

535 Region ‘A’ represents the unjammed state since $Z < Z_{jam}$. However, we didn’t find any
 536 data exists in ‘A’ based on our present and previous simulations. The fabric state for jammed
 537 specimens jumps from $Z > Z_{jam}$ to the origin of coordinates upon unjamming (or liquefaction)
 538 irrespective of whether it is induced by monotonic or cyclic shearing, and the fabric state of
 539 liquefied specimens jumps from ‘Flow transient’ to the origin of coordinates upon loading
 540 reversals.³³ Further investigations are needed to determine whether region ‘A’ is truly
 541 inaccessible for quasi-statically sheared granular materials.

542 In all of our simulations, region ‘C’ characterized by high F values has never been
 543 reached and is deemed to be inaccessible. For a fixed coordination number, large F means all
 544 contacts are aligned along one direction but not supported laterally. This could result in the
 545 buckling of the force chain and thus unstable contact network, providing an explanation for
 546 the lack of fabric states in “C” for granular materials at the quasi-static limit. The
 547 accessibility of fabric states due to local geometrical constraints has been also discussed in
 548 analytical settings³⁴.

549 Identifying the fabric characteristics underlying different phases creates the possibility to
 550 determine the state of granular materials solely through kinematical measures such as optical
 551 methods or X-ray tomography without the need to ascertain the stress state of the specimen.
 552 In industrial applications, gaining access to the stress state within a granular flow undergoing

553 complex boundary conditions is usually impractical.⁸² Utilizing geometry-based methods to
 554 identify phase states can provide valuable insights into the efficiency of granular system and
 555 serve as a guide for future optimization efforts. Furthermore, the fabric-based phase diagram
 556 (Fig. 8) can furnish insights into whether a granular packing is at a transient state or has
 557 attained a final steady state, which serves as a valuable feature in geoscience studies in
 558 determining the shear history of granular materials in certain regions (e.g., fault gauge).^{83, 84}

559 **5. Fabric – f_{nr} relation**

560 Fig.9 investigates the relation between contact fabrics and the non-rattler fraction f_{nr} . It
 561 is observed from Fig. 9(a) that all the $Z_{nr} - f_{nr}$ data fall within a narrow band. Similar
 562 observation has been reported from pure shear photoelastic experiments.^{9, 85} This suggests
 563 that Z_{nr} and f_{nr} maintain a robust relationship that presents in both 2D and 3D granular
 564 specimens. The total coordination number Z_t appears to correlate even better with f_{nr} as
 565 shown in Fig. 9(c). All data effectively collapse into a curve, regardless of whether the
 566 sample being UJ, F/SJ, or J throughout the shearing process. By plotting the $Z - f_{nr}$ data of
 567 only unjammed specimens in the subplots of Figs. 9(a)(c), we confirm that the sample
 568 remains unjammed when $f_{nr} < 0.855$ but will enter F/SJ or J phases once f_{nr} exceeds this
 569 value.

570 Figs. 9(b)(d) show that the normalized fabric anisotropy $\bar{F}_{nr} = F_{nr} / Z_{nr}$ and $\bar{F}_t = F_t / Z_t$
 571 decrease as f_{nr} increases, confirming that denser and more jammed granular packings develop
 572 less normalized fabric anisotropy.^{21, 32} Similar to the $Z - f_{nr}$ plots, all the $\bar{F}_{nr} - f_{nr}$ and $\bar{F}_t - f_{nr}$
 573 data collapse into a narrow band. The correlation is improved for the steady-state data as
 574 shown in the subplots of Figs. 9(b)(d). It shows that the steady-state $\bar{F}_{nr} - f_{nr}$ and $\bar{F}_t - f_{nr}$
 575 lines are essentially identical. Furthermore, in Fig. 9(e), the correlation between the steady-
 576 state normalized fabric anisotropy $\bar{F}_{nr, st}$ and $\bar{F}_{t, st}$ data is striking similar, clustering around
 577 the around the 1:1 line with $R^2 = 0.9985$, although $\bar{F}_{t, st}$ contains extra fabric data about the
 578 rattlers. This suggests that the contact network of rattlers in the steady state is not random or

579 isotropic; instead, it aligns with the same major direction or anisotropy as that of the non-
 580 rattler contact network. To demonstrate this, Fig.10 presents the polar histogram of non-
 581 rattler- and rattler- contact normals' probability distribution density in y - z plane of the
 582 specimen with $\phi = 0.57$ at $\gamma = 0, 0.2, 1.0$ and 2.0 , respectively. In Fig. 10, the radius of each
 583 bin represents the (number of contact normals in the bin) / (number of all contact normals) /
 584 (width of each bin, i.e., $20^\circ = 0.3491$ rad). Fig. 10 (a)-(d) shows that the non-rattler contact
 585 network initially does not exist, then begins to exhibit some degree of anisotropy at $\gamma = 0.2$,
 586 followed by a slight decrease as it stabilizes into a steady state. This pattern is consistent with
 587 the observations in Fig. 6(b). On the other hand, Fig. 10 (e)-(h) shows that a random rattler-
 588 contact network exists prior to shearing. As shearing proceeds, a distinct level of anisotropy
 589 emerges within the rattler contact distribution, and this anisotropy aligns with a direction akin
 590 to that observed in the non-rattler contact network.

591 **6. Concluding remarks**

592 This study investigates the fabric structure of frictional granular materials near jamming
 593 transition through a series of constant- ϕ quasi-static simple shear DEM tests. The fabric
 594 structure characterized by three different contact networks is analyzed in terms of
 595 coordination number (Z), fabric anisotropy (F), and non-rattler fraction (f_{nr}). A unifying
 596 Critical Fabric Surface (CFS) for both unjammed (UJ) and jammed (F/SJ, J) granular
 597 packings is found in F - Z plane. In addition, a novel jamming phase diagram in the fabric F - Z
 598 plane is proposed, and its potential applications are discussed. The main conclusions of this
 599 study are summarized below:

- 600 (1) The boundary between the unjammed and jammed phases in the JPD within the p - ϕ
 601 plane is equivalent to the critical state line frequently discussed in soil mechanics
 602 literature within the e - p plane. In addition, the p - ϕ JPD should incorporate a densest
 603 state line at higher ϕ values. Beyond this line, states become inaccessible unless certain
 604 processes, such as grain crushing, begin to modify the grain size distribution and the
 605 grain morphology.
- 606 (2) By plotting the fabric paths of all samples on the F - Z plane, we identified a unique CFS

607 that attracts the fabric state (including the non-rattler, total, and strong contact
608 networks) of granular assemblies upon shearing. This observation underscores that a
609 steady-state granular flow with $\phi > \phi_G$ consistently exhibits microstructural anisotropy,
610 irrespective of whether it is jammed or unjammed.

611 (3) We proposed a conceptual JPD in the fabric F - Z space. The fabric JPD provides a
612 geometrical metric for assessing the phase state of granular materials, complementing
613 the conventional JPD in which information regarding the stress state of the assembly is
614 necessary. This approach offers a fresh perspective for understanding the jamming
615 phenomenon, potentially serving as a source of inspiration for researchers in both
616 granular physics and geomechanics.

617 (4) Our simulation shows a one-to-one relation between the non-rattler fraction f_{nr} and the
618 coordination numbers Z_t and Z_{nr} for all samples throughout shearing. The rattler
619 particles do not exhibit an isotropic distribution during shearing; instead, they tend to
620 align along the direction where the total fabric anisotropy emerges. A threshold non-
621 rattler fraction $f_{nr,jam} = 0.855$ that separates jammed and unjammed packings is
622 identified. This value is close to 0.83 that was identified in prior 2D photoelastic
623 experiments.⁹

624 One limitation of the present study is that the fragile and shear jammed states are not
625 distinguished due to the absence of stress reversal in the loading program and also the lack of
626 a quantitative definition of fragile. The JPDs constructed in this study therefore do not
627 separate the fragile and the shear jammed phases in both the conventional τ - ϕ space and the
628 fabric F - Z space. The clarification between different criteria for the determination of
629 fragile and precise determination of its region in the phase diagram worth a systematic study,
630 which is one of the primary goals in our follow up studies. An additional limitation is the
631 omission of highly stochastic characteristics in the unjamming-jamming transition within the
632 current simulation, which is known to be significantly influenced by finite size effects. The
633 statistical uncertainties in determining the jamming/unjamming boundary in the JPD requires
634 further refinement to clearly elucidate this aspect in future investigations.

635 **Author contributions**

636 Yuxuan Wen conducted the simulation, performed the analysis, and drafted the manuscript.

637 Yida Zhang initiated the conceptualization, secured funding, provided supervision, and

638 revised the manuscript.

639 **Conflicts of interest**

640 There are no conflicts of interest to declare

641 **Acknowledgements**

642 This research was supported by the U.S. National Science Foundation (NSF) under NSF

643 CMMI Award No. 2237332 and the Predictive Science Academic Alliance Program

644 (PSAAP) under Award No. DE-NA0003962. The authors would also like to acknowledge Dr.

645 Yiqiu Zhao (currently at Hong Kong University of Science and Technology) for the

646 enormous help and constructive discussions throughout this study.

647 **References**

- 648 1. J. Liu and S. R. Nagel, *Nature*, 1998, **396**, 21-22.
- 649 2. R. P. Behringer, *Comptes Rendus Physique*, 2015, **16**, 10-25.
- 650 3. R. P. Behringer and B. Chakraborty, *Reports on Progress in Physics*, 2019, **82**,
651 012601.
- 652 4. C. S. O'Hern, S. A. Langer, A. J. Liu and S. R. Nagel, *Physical Review Letters*, 2002,
653 **88**, 075507.
- 654 5. C. S. O'Hern, L. E. Silbert, A. J. Liu and S. R. Nagel, *Physical Review E*, 2003, **68**,
655 011306.
- 656 6. T. S. Majmudar and R. P. Behringer, *Nature*, 2005, **435**, 1079-1082.
- 657 7. H. P. Zhang and H. A. Makse, *Physical Review E*, 2005, **72**, 011301.
- 658 8. L. E. Silbert, *Soft Matter*, 2010, **6**, 2918-2924.
- 659 9. D. Bi, J. Zhang, B. Chakraborty and R. P. Behringer, *Nature*, 2011, **480**, 355-358.
- 660 10. C. Song, P. Wang and H. A. Makse, *Nature*, 2008, **453**, 629-632.
- 661 11. G. Y. Onoda and E. G. Liniger, *Physical Review Letters*, 1990, **64**, 2727-2730.
- 662 12. S. Luding, *Nature Physics*, 2016, **12**, 531-532.
- 663 13. M. E. Cates, J. P. Wittmer, J. P. Bouchaud and P. Claudin, *Physical Review Letters*,
664 1998, **81**, 1841-1844.
- 665 14. Y. Zhao, J. Barés, H. Zheng, J. E. S. Socolar and R. P. Behringer, *Physical Review*
666 *Letters*, 2019, **123**, 158001.
- 667 15. F. Radjai, M. Jean, J.-J. Moreau and S. Roux, *Physical Review Letters*, 1996, **77**, 274-
668 277.
- 669 16. D. M. Mueth, H. M. Jaeger and S. R. Nagel, *Physical Review E*, 1998, **57**, 3164-3169.
- 670 17. C. S. O'Hern, S. A. Langer, A. J. Liu and S. R. Nagel, *Physical Review Letters*, 2001,
671 **86**, 111-114.
- 672 18. M. Oda, *Soils and Foundations*, 1972, **12**, 45-63.
- 673 19. F. Radjai, D. E. Wolf, M. Jean and J.-J. Moreau, *Physical Review Letters*, 1998, **80**,
674 61-64.
- 675 20. L. Rothenburg and R. J. Bathurst, *Géotechnique*, 1989, **39**, 601-614.
- 676 21. J. Zhao and N. Guo, *Géotechnique*, 2013, **63**, 695-704.
- 677 22. I. Srivastava, L. E. Silbert, G. S. Grest and J. B. Lechman, *Physical Review Letters*,
678 2019, **122**, 048003.
- 679 23. I. Srivastava, L. E. Silbert, J. B. Lechman and G. S. Grest, *Soft Matter*, 2022, **18**, 735-
680 743.
- 681 24. M. Wiebicke, E. Andò, G. Viggiani and I. Herle, *Acta Geotechnica*, 2020, **15**, 79-93.
- 682 25. W. H. Imseeh, A. M. Druckrey and K. A. Alshibli, *Granular Matter*, 2018, **20**, 24.
- 683 26. A. N. Schofield and C. P. Wroth, *Critical State Soil Mechanics*, McGraw-hill,
684 London, 1968.
- 685 27. X. S. Li and Y. F. Dafalias, *Journal of Engineering Mechanics*, 2012, **138**, 263-275.
- 686 28. J. Zhao and Z. Gao, *Journal of Engineering Mechanics*, 2016, **142**, 04015056.
- 687 29. D. Liao and Z. Yang, *International Journal for Numerical and Analytical Methods in*

- 688 *Geomechanics*, 2021, **45**, 2433-2463.
- 689 30. Y. Zhang, X. Zhou and Y. Wen, *Journal of Engineering Mechanics*, 2020, **146**,
690 04020019.
- 691 31. M. Otsuki and H. Hayakawa, *Physical Review E*, 2020, **101**, 032905.
- 692 32. Y. Wen and Y. Zhang, *Géotechnique*, 2023, **73**, 439-454.
- 693 33. Y. Wen and Y. Zhang, *Acta Geotechnica*, 2022, **17**, 4297-4312.
- 694 34. F. Radjai, J. Y. Delenne, E. Azéma and S. Roux, *Granular Matter*, 2012, **14**, 259-264.
- 695 35. V. Trappe, V. Prasad, L. Cipelletti, P. N. Segre and D. A. Weitz, *Nature*, 2001, **411**,
696 772-775.
- 697 36. Z. Zhang, N. Xu, D. T. N. Chen, P. Yunker, A. M. Alsayed, K. B. Aptowicz, P.
698 Habdas, A. J. Liu, S. R. Nagel and A. G. Yodh, *Nature*, 2009, **459**, 230-233.
- 699 37. M. P. Ciamarra, R. Pastore, M. Nicodemi and A. Coniglio, *Physical Review E*, 2011,
700 **84**, 041308.
- 701 38. A. J. Liu and S. R. Nagel, *Annual Review of Condensed Matter Physics*, 2010, **1**, 347-
702 369.
- 703 39. V. Šmilauer, V. Angelidakis, E. Catalano, R. Caulk, B. Chareyre, W. Chèvremont, S.
704 Dorofeenko, J. Duriez, N. Dyck, J. Eliáš, B. Er, A. Eulitz, A. Gladky, N. Guo, C.
705 Jakob, F. Kneib, J. Kozicki, D. Marzougui, R. Maurin, C. Modenese, G. Pekmezi, L.
706 Scholtès, L. Sibille, J. Stránský, T. Sweijen, K. Thoeni and C. Yuan, 2021, DOI:
707 10.5281/zenodo.5705394.
- 708 40. S. R. Williams, C. P. Royall and G. Bryant, *Physical Review Letters*, 2008, **100**,
709 225502.
- 710 41. M. v. Hecke, *Journal of Physics: Condensed Matter*, 2010, **22**.
- 711 42. M. P. Ciamarra and A. Coniglio, *Physical Review Letters*, 2009, **103**, 235701.
- 712 43. J. K. Mitchell and K. Soga, *Fundamentals of soil behavior*, Wiley, New York, 3rd
713 edn., 2005.
- 714 44. M. R. Kuhn, W. Sun and Q. Wang, *Acta Geotechnica*, 2015, **10**, 399-419.
- 715 45. X. Gu, M. Huang and J. Qian, *Granular Matter*, 2014, **16**, 91-106.
- 716 46. G. Wang and J. Wei, *Granular Matter*, 2016, **18**, 1-13.
- 717 47. C. E. Maloney and A. Lemaître, *Physical Review E*, 2006, **74**, 016118.
- 718 48. D. Fiocco, G. Foffi and S. Sastry, *Physical Review E*, 2013, **88**, 020301.
- 719 49. Z. Shojaaee, L. Brendel, J. Török and D. E. Wolf, *Physical Review E*, 2012, **86**,
720 011302.
- 721 50. Z. Shojaaee, J.-N. Roux, F. Chevoir and D. E. Wolf, *Physical Review E*, 2012, **86**,
722 011301.
- 723 51. P. Schuhmacher, F. Radjai and S. Roux, presented in part at the EPJ Web of
724 Conferences, 2017.
- 725 52. J. Christoffersen, M. M. Mehrabadi and Nemat-Nasser, *Journal of Applied*
726 *Mechanics*, 1981, **48**.
- 727 53. R. D. Mindlin and H. Deresiewicz, *Journal of Applied Mechanics*, 1953, **20**, 327-344.
- 728 54. Y. H. Xie, Z. X. Yang, D. Barreto and M. D. Jiang, *Granular Matter*, 2017, **19**, 35.
- 729 55. P. A. Cundall, in *Analytical and computational methods in engineering rock*

- 730 *mechanics*, ed. E. T. Brown, Allen & Unwin, London, 1987, pp. 129-163.
- 731 56. B. Chareyre and P. Villard, *Journal of Engineering Mechanics*, 2005, **131**, 689-698.
- 732 57. P. Fu and Y. F. Dafalias, *International Journal for Numerical and Analytical Methods*
733 *in Geomechanics*, 2011, **35**, 1918-1948.
- 734 58. X. Li and X. S. Li, *Journal of Engineering Mechanics*, 2009, **139**, 641-656.
- 735 59. K. Kanatani, *International journal of Engineering Science*, 1984, **22**, 149-164.
- 736 60. C. Heussinger and J.-L. Barrat, *Physical Review Letters*, 2009, **102**, 218303.
- 737 61. P. Rissone, E. I. Corwin and G. Parisi, *Physical Review Letters*, 2021, **127**, 038001.
- 738 62. I. Srivastava, L. E. Silbert, G. S. Grest and J. B. Lechman, *Journal of Fluid*
739 *Mechanics*, 2021, **907**, A18.
- 740 63. R. Seto, A. Singh, B. Chakraborty, M. M. Denn and J. F. Morris, *Granular Matter*,
741 2019, **21**, 82.
- 742 64. S. Chen, T. Bertrand, W. Jin, M. D. Shattuck and C. S. O'Hern, *Physical Review E*,
743 2018, **98**, 042906.
- 744 65. H. A. Vinutha and S. Sastry, *Nature Physics*, 2016, **12**, 578-583.
- 745 66. A. P. Santos, D. S. Bolintineanu, G. S. Grest, J. B. Lechman, S. J. Plimpton, I.
746 Srivastava and L. E. Silbert, *Physical Review E*, 2020, **102**, 032903.
- 747 67. A. Donev, S. Torquato, F. H. Stillinger and R. Connelly, *Journal of Computational*
748 *Physics*, 2004, **197**, 139-166.
- 749 68. A. H. Clark, J. D. Thompson, M. D. Shattuck, N. T. Ouellette and C. S. O'Hern,
750 *Physical Review E*, 2018, **97**, 062901.
- 751 69. K. H. Roscoe, A. N. Schofield and C. P. Wroth, *Géotechnique*, 1958, **8**, 22-53.
- 752 70. M. Cubrinovski and K. Ishihara, *Soils and Foundations*, 2002, **42**, 65-78.
- 753 71. C. S. Chang, Y. Deng and Z. Yang, *Journal of Engineering Mechanics*, 2017, **143**,
754 04017060.
- 755 72. M. A. Maroof, A. Mahboubi, E. Vincens and A. Noorzad, *Granular Matter*, 2022, **24**,
756 41.
- 757 73. K. Ishihara, *Soil behaviour in earthquake geotechnics*, Clarendon Press, Oxford,
758 1996.
- 759 74. Z. X. Yang and K. Pan, *Soil Dynamics and Earthquake Engineering*, 2017, **92**, 68-78.
- 760 75. J. Barés, D. Wang, D. Wang, T. Bertrand, C. S. O'Hern and R. P. Behringer, *Physical*
761 *Review E*, 2017, **96**, 052902.
- 762 76. G.-C. Cho, J. Dodds and J. C. Santamarina, *Journal of Geotechnical and*
763 *Geoenvironmental Engineering*, 2006, **132**, 591-602.
- 764 77. A. Tengattini, A. Das and I. Einav, *Géotechnique*, 2016, **66**, 695-710.
- 765 78. Y. D. Zhang, G. Buscarnera and I. Einav, *Géotechnique*, 2016, **66**, 149-160.
- 766 79. R. Wang, P. Fu, J.-M. Zhang and Y. F. Dafalias, *Acta Geotechnica*, 2016, **11**, 1321-
767 1337.
- 768 80. É. Guazzelli and O. Pouliquen, *Journal of Fluid Mechanics*, 2018, **852**, P1.
- 769 81. D. Gunary, *Journal of Soil Science*, 1970, **21**, 72-77.
- 770 82. A. Janda, I. Zuriguel and D. Maza, *Physical Review Letters*, 2012, **108**, 248001.
- 771 83. C. D. Rowe, J. C. Moore, F. Meneghini and A. W. McKeirnan, *Geology*, 2005, **33**,

- 772 937-940.
- 773 84. A.-M. Boullier, E.-C. Yeh, S. Boutareaud, S.-R. Song and C.-H. Tsai, *Geochemistry,*
774 *Geophysics, Geosystems*, 2009, **10**.
- 775 85. J. Ren, PhD PhD Dissertation, Duke University, 2013.
- 776

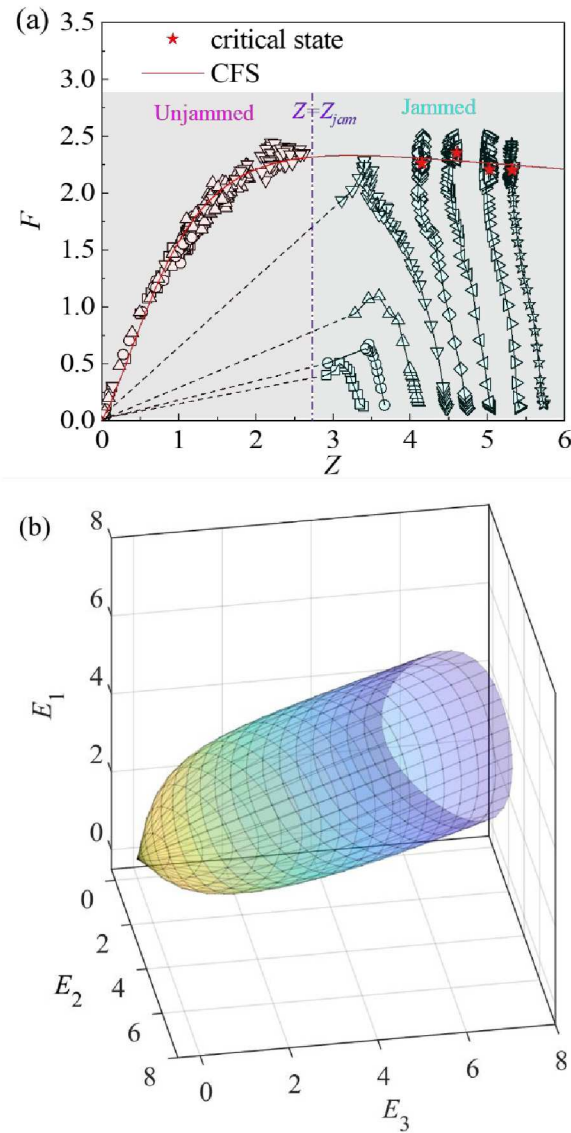


Fig. 1. (a) Critical fabric surface (CFS) and fabric evolution in F - Z plane and (b) CFS in principal fabric space, adapted from ref. 30. Z is coordination number; F characterizes fabric anisotropy; E_1 , E_2 and E_3 are the major, intermediate, and minor principal values of fabric tensor E_{ij} , which can be calculated using Eqs. (7) and (9). All data were obtained from DEM simulations of constant- ϕ triaxial test on three-dimensional (3D) spherical particles. Samples were first isotropically compressed to different confining pressures, producing an initially jammed (Z 's $> Z_{jam}$) and isotropic (F 's ≈ 0) state. They are then subjected to constant- ϕ , quasi-static true triaxial shearing. Fig. 1(a) shows all fabric paths evolve to a final CFS (red line). During shearing, several specimens' fabric state (Z , F) abruptly jumped to the origin (denoted by dashed lines), experiencing sudden unjamming. With continuous application of shear strain, their fabric states evolve away from the origin following the CFS in the $Z < Z_{jam}$ range. Fig. 1(b) compiles the CFS for all true triaxial tests conducted at different Lode angles, giving a 3D CFS in the principal fabric space.

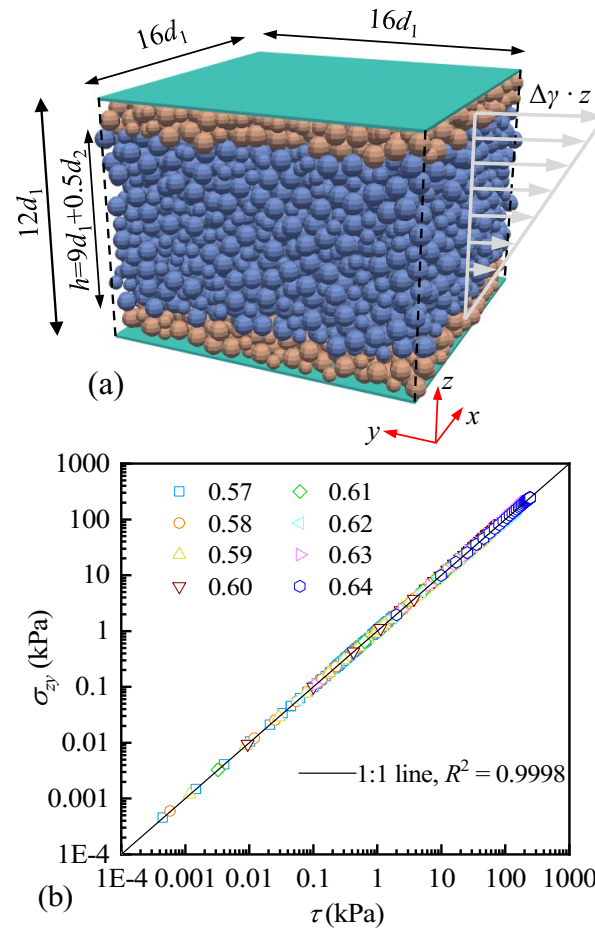


Fig. 2. Constant volume simple shear test: (a) sample during shear, where orange particles are the clumped particle-walls to impart non-trivial shear stress to the sheared particles while simultaneously preventing the escape of particles from the simulation region. Note that the simulation does not employ a wall-driven shearing algorithm. Instead, the shear strain is applied affinely to each individual particle and the two particle-walls. This is accomplished by assigning the displacement of each object directly through the utilization of the vertical coordinate and the constant shear strain increment during each timestep, followed by a subsequent relaxation stage; (b) Calibration of the effective height h of the specimen under shear.

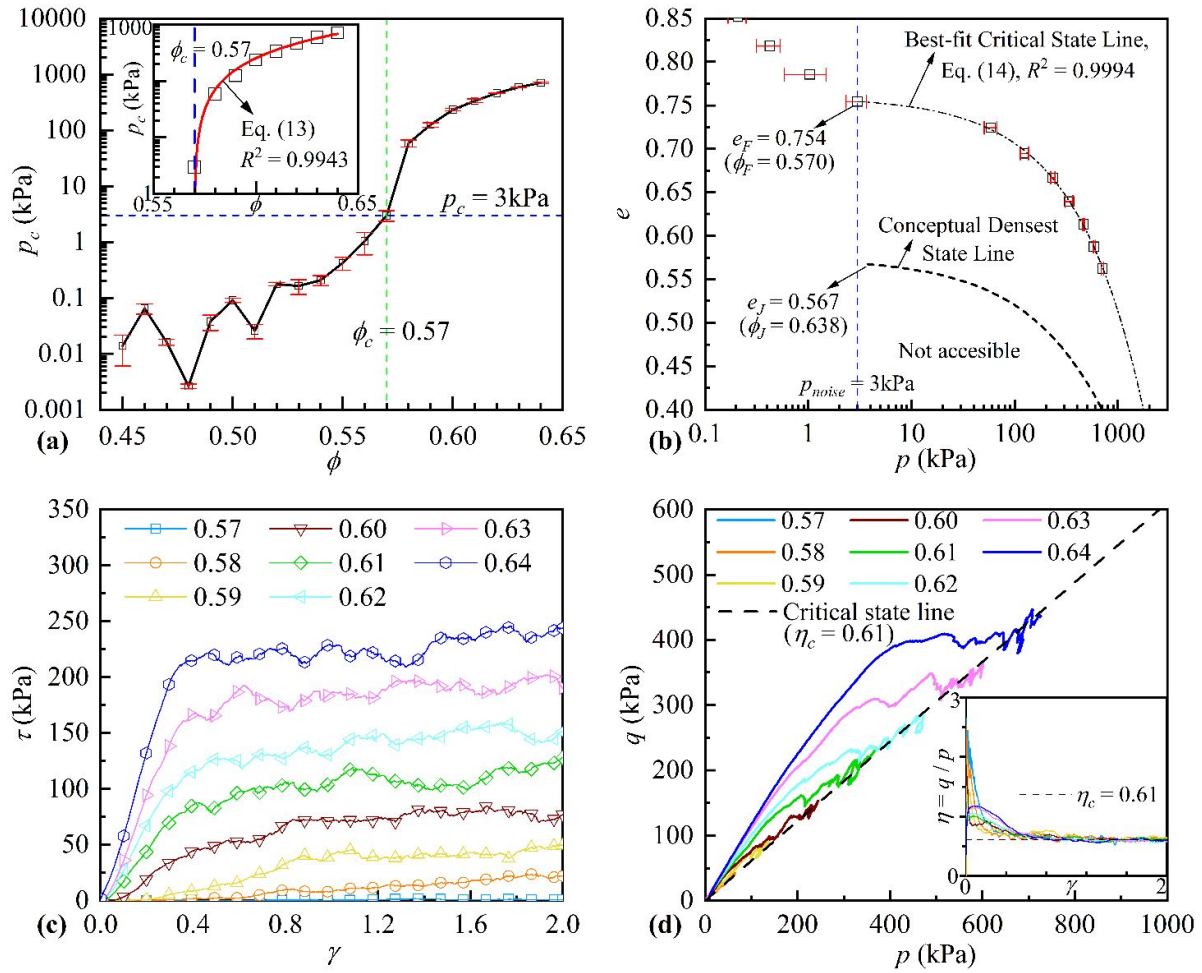


Fig. 3. Jamming thresholds in stress space: (a) determination of ϕ_F and p_{noise} ; (b) determination of ϕ_J , the best-fit critical state line, and the sketched densest state line; (c) stress-strain evolution of (shear) jammed specimens; (d) stress paths and critical state stress ratio.

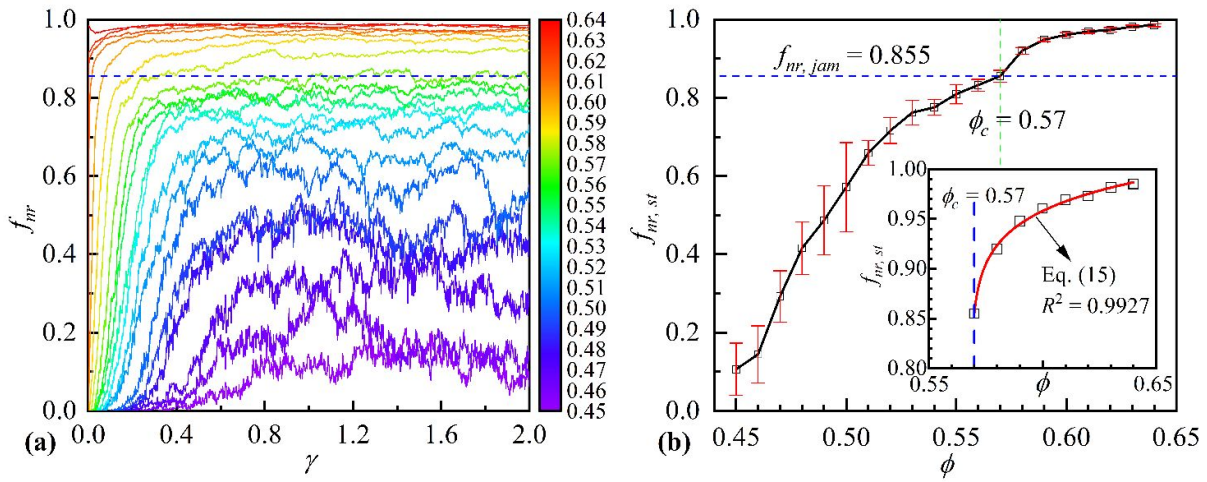


Fig. 4. Non-rattler fraction f_{nr} : (a) evolution with respect to shear strain; (b) steady-state values.

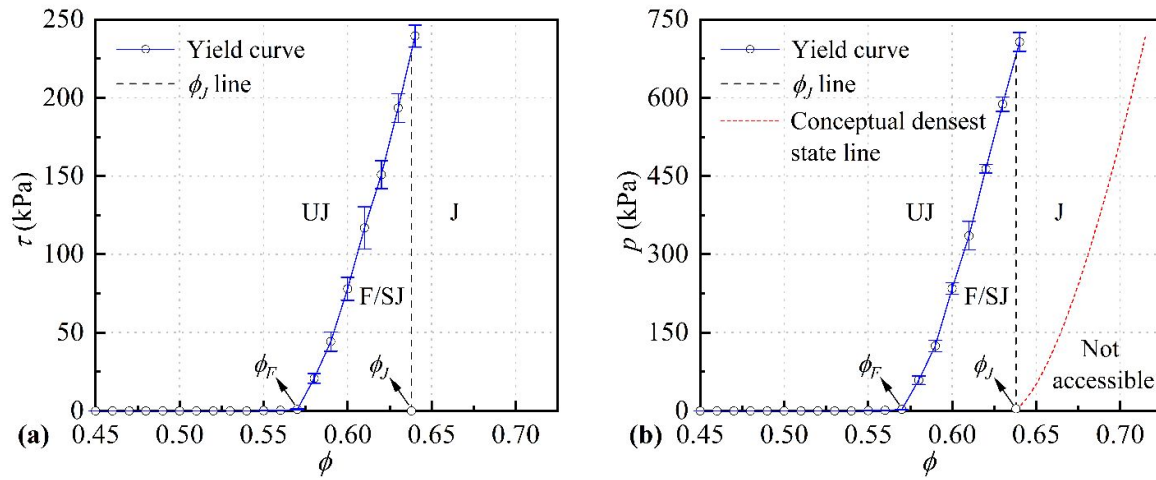


Fig. 5. Classical jamming phase diagram: (a) in τ - ϕ plane and (b) in p - ϕ plane.

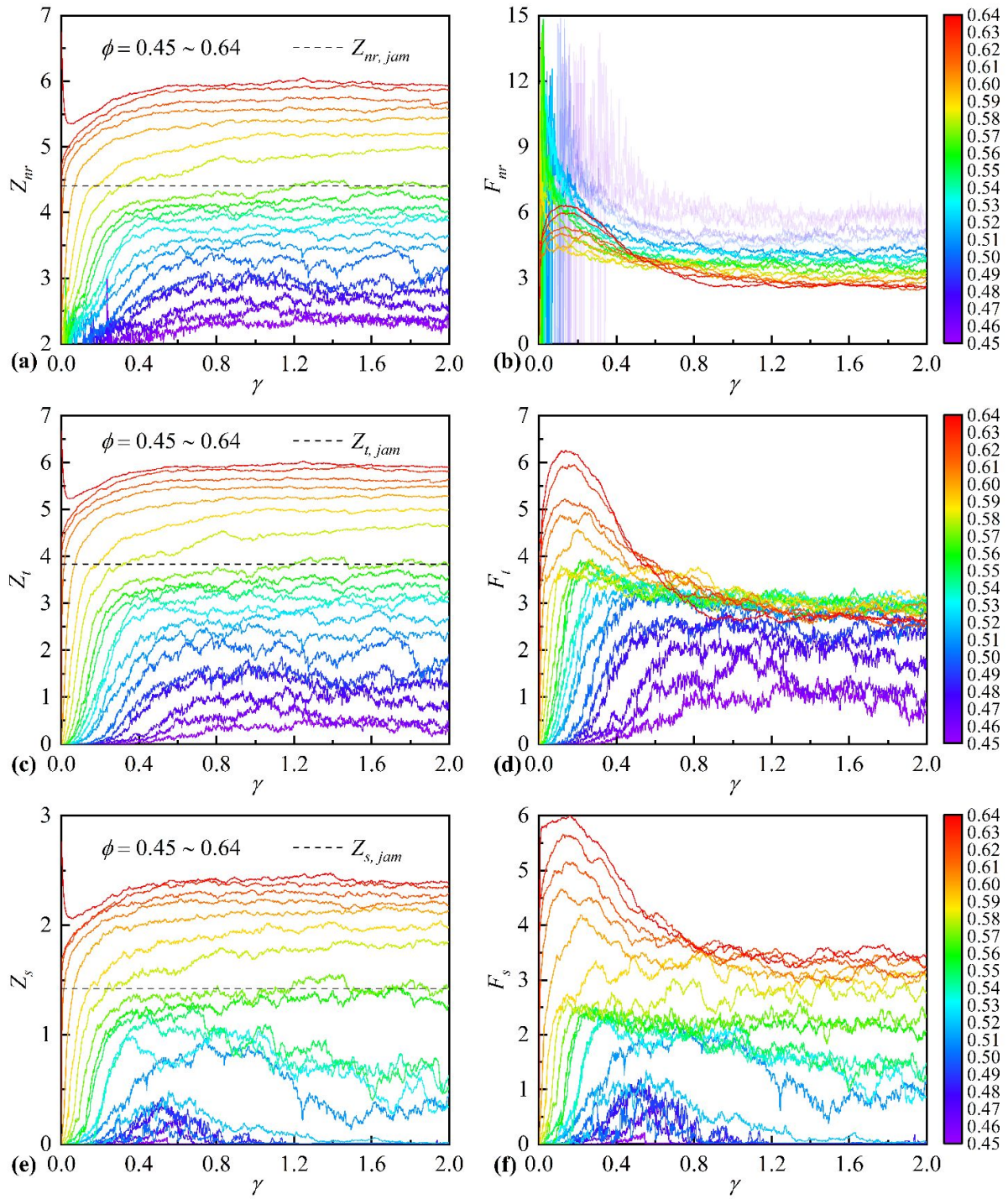


Fig. 6. Evolution of coordination numbers and fabric anisotropies: (a), (c) and (e) the evolution of Z_{nr} , Z_t and Z_s with respect to γ ; (b), (d) and (f) the evolution of F_{nr} , F_t and F_s with respect to γ .

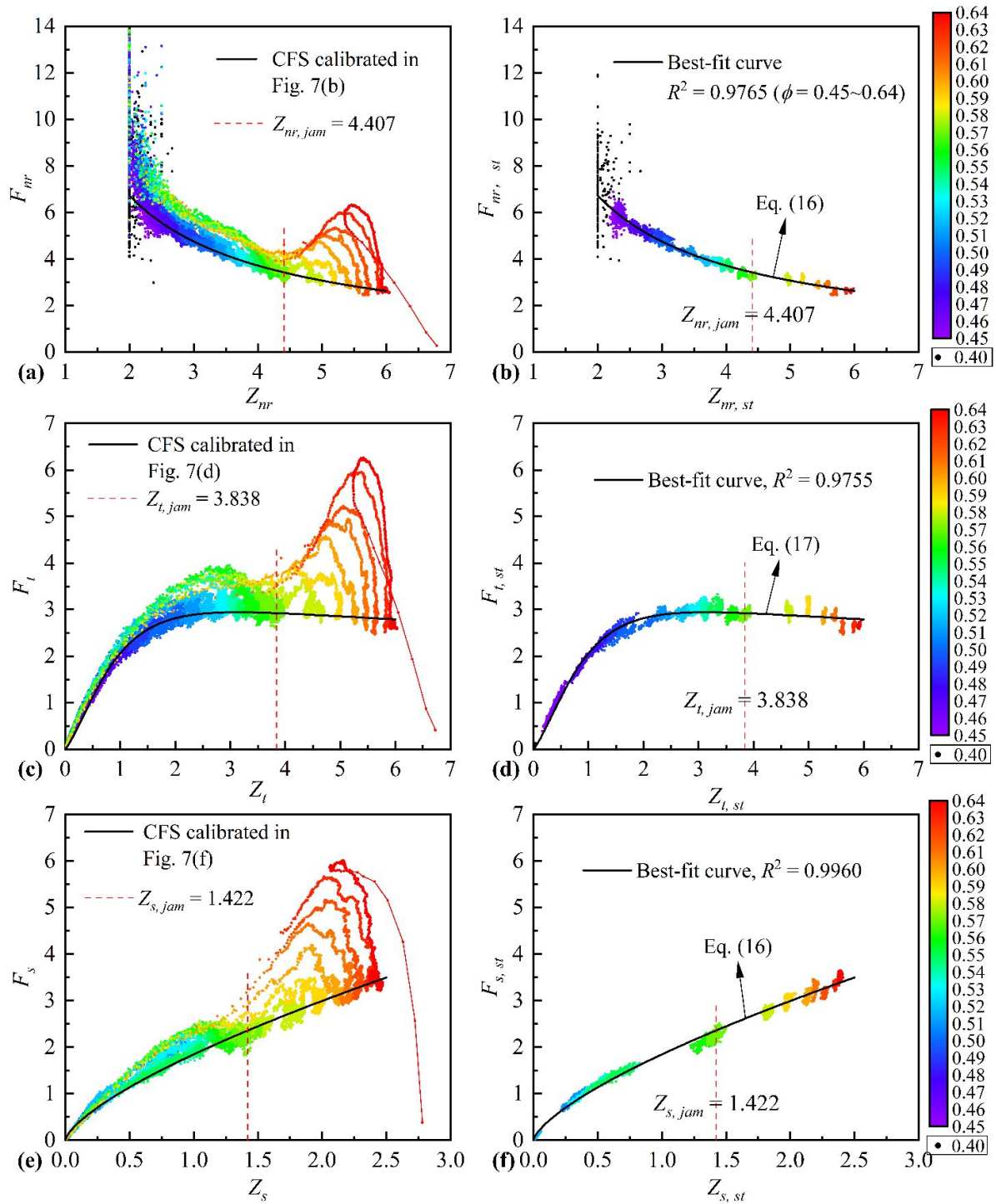


Fig. 7. Fabric paths and critical fabric surface in the F - Z plane: non-rattler fabric (a) paths and (b) CFS; total fabric (c) paths (d) CFS; strong fabric (e) paths and (f) CFS.

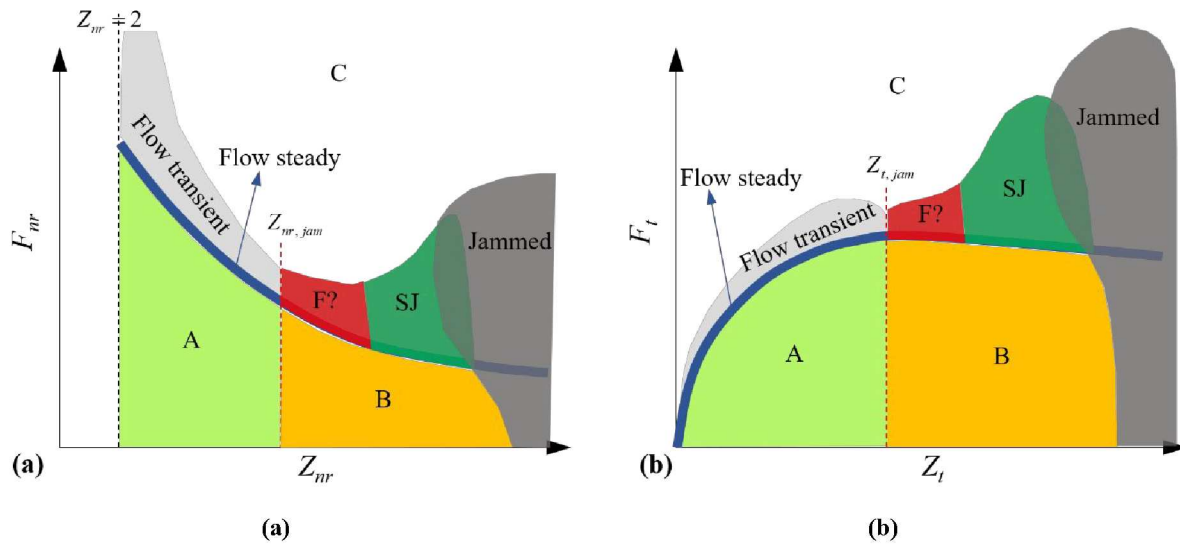


Fig. 8. Jamming phase diagram mapped to the fabric F - Z space: (a) non-rattler fabric; (b) total fabric.

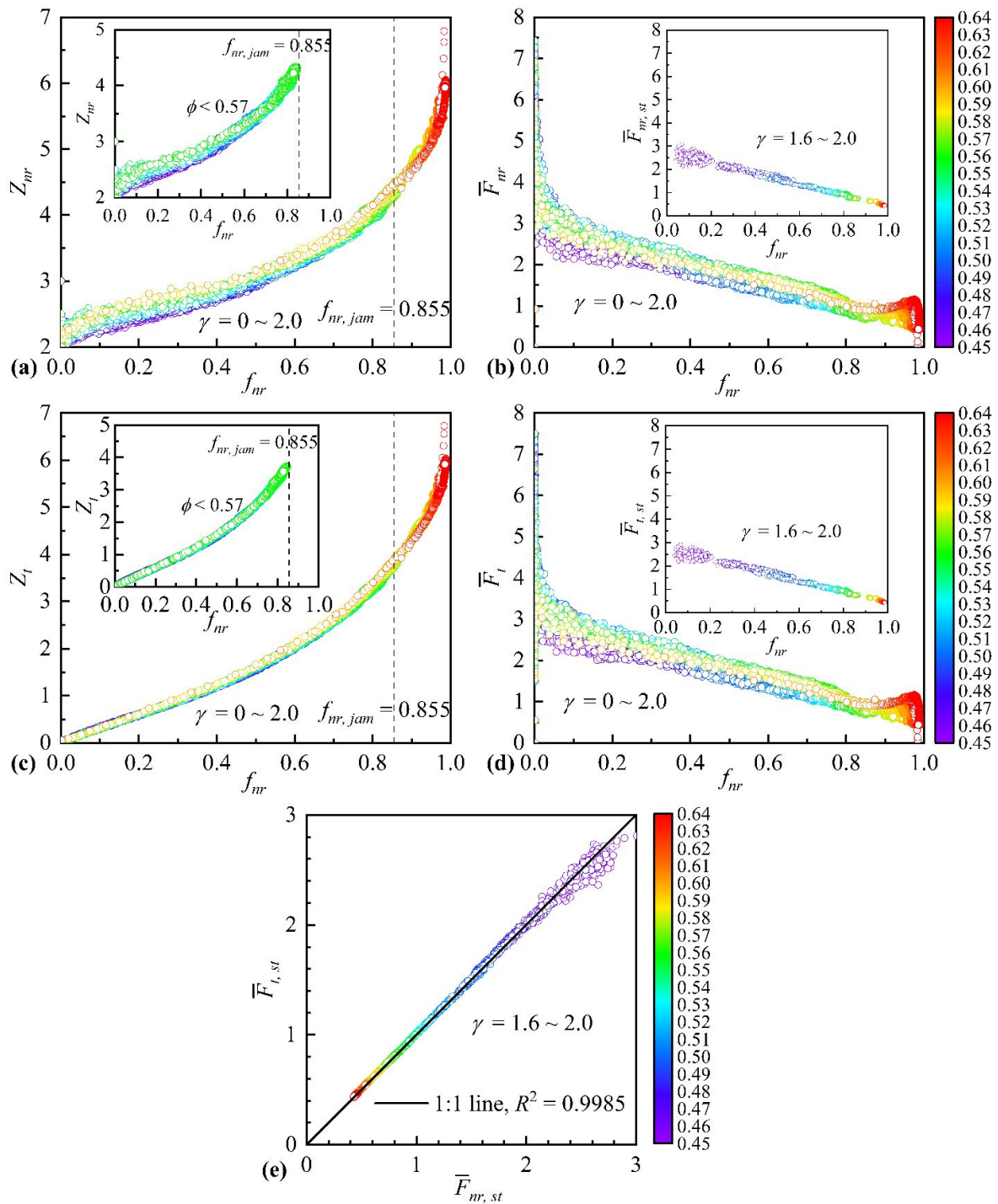


Fig. 9. Evolution of fabrics with respect to f_{nr} : (a) and (c) report the evolution of Z_{nr} , Z_t , where the subplots present the data of unjammed specimens only; (b) and (d) report the evolution of \bar{F}_{nr} and \bar{F}_t , where the subplots show the steady state data only; (e) comparison between steady state non-rattler and total contact normalized fabric anisotropies.

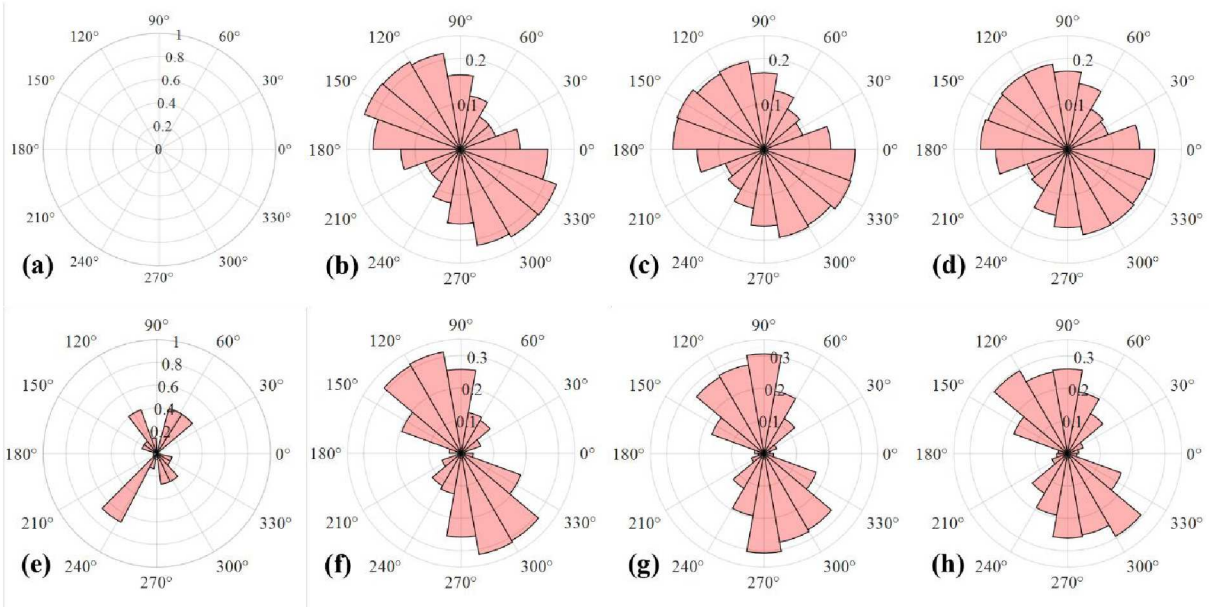
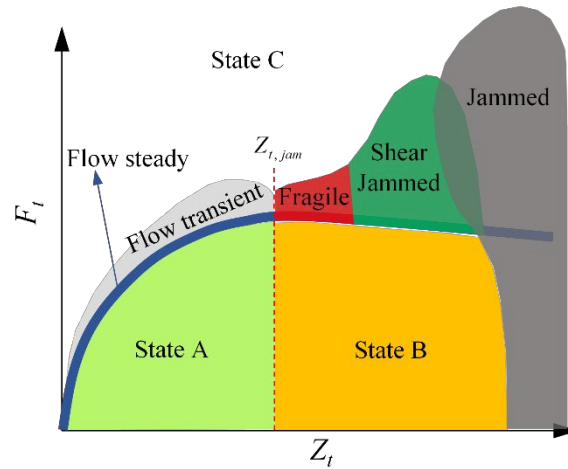


Fig. 10. Contact probability distribution density of $\phi = 0.57$ in y - z plane: (a)-(d) non-rattler contacts at $\gamma = 0, 0.2, 1.0$ and 2.0 , respectively; (e)-(f) rattler contacts at $\gamma = 0, 0.2, 1.0$ and 2.0 , respectively. The radius of each bin represents the (number of contact normals in the bin) / (number of all contact normals) / (width of each bin, i.e., $20^\circ = 0.3491$ rad).



Fabric-based jamming phase diagram for frictional granular materials, where F_t and Z_t are the fabric anisotropy (deviatoric invariant of the 2nd order fabric tensor) and the coordination number (mean invariant of the 2nd order fabric tensor) of the total-contact network, respectively.